AN ABSTRACT OF THE THESIS OF

Julius O. Orwa for the degree of Master of Science in Physics

presented on October 27, 1989.

Title: Two Dimensional Electron Transport in Pseudomorphic InGaAs/AlGaAs Heterojunctions

Redacted for Privacy

Abstract approved: _____
Dr. Stephen M. Goodnick

Pseudomorphic InGaAs/AlGaAs heterostructures have demonstrated superior device performance than the much more widely studied GaAs/AlGaAs system. The last decade has therefore seen an increased interest in the former system although, to date, a complete understanding of the transport charasteristics of this material is still lacking. In particular, alloy scattering, which is thought to be important in this system at low temperatures, is at best vaguely understood.

In the present study, transport properties of pseudomorphic $In_xGa_{1-x}As/Al_yGa_{1-y}As$ heterojunctions are investigated for two samples with $x = 0.15$ and $x = 0.25$. The corresponding values of y are 0.2 and 0.25, respectively. Among the parameters determined are the mobility and channel carrier concentration as functions of temperature from 2 °K to 300 °K using the techniques of low field Hall effect and high field magnetoconductance. A theoretical explanation of the temperature dependence of the mobility based on the scattering mechanisms in the channel is attempted. Qualitative agreement is obtained between theory and experiment but the experimental curve is found to be lower at all

temperatures. In addition, the channel electron effective mass is determined from the temperature dependence of the high field oscillatory magnetoconductance amplitude. An apparent field dependence of the mass is observed but is not fully accounted for by the many body theory that addresses field dependence.

TWO DIMENSIONAL ELECTRON TRANSPORT IN PSEUDOMORPHIC InGaAs/AlGaAs HETEROJUNCTIONS

by

Julius O. Orwa

A THESIS

Submitted to

Oregon State University

in partial fulfillment of
the requirements for the
degree of

Master of Science

Completed October 27, 1989

Commencement June 1990

APPROVED:

Redacted for Privacy

Professor of Physics in charge of major

Redacted for Privacy

Head of department of Physics

Redacted for Privacy

Dean of Graduate School

Date thesis is presented October 27, 1989

Typed by researcher for Julius O. Orwa

ACKNOWLEDGEMENTS

I extend my deepest gratitude to my advisor, Dr. Stephen M. Goodnick for guidance and encouragement through many difficult steps during the writing of this manuscript. Special thanks go to Dr. Allen Wasserman with whom I had several discussions on certain theoretical aspects of the subject. I would also like to thank Hyungmoo Yoo, John Ebner, and Jenifer Lary for technical assistances at various stages during the preparation of the manuscript.

My final thanks go to Bruce Odekirk of TriQuint Semiconductor for providing one of the samples used in the study.

TABLE OF CONTENTS

LIST OF FIGURES

LIST OF FIGURES

LIST OF TABLES

TWO DIMENSIONAL ELECTRON TRANSPORT IN PSEUDOMORPHIC InGaAs/AlGaAs HETEROJUNCTIONS

I. INTRODUCTION

Society relies heavily on information processing and a great deal of effort has been devoted to perfecting this technology. One of the major concerns has been to develop data processing machines with increasingly greater speeds to keep up with the demands that arise from the constantly increasing size and complexity of tasks required. The rate of information processing depends on the switching speeds of various component devices that constitute a system. Switching speed is dependent on the effective transit time for charge through a given device and is limited by both the device dimensions and individual material properties which determine the carrier mobility and drift velocity. The former limitation has largely been dealt with to practical limits through device miniaturization. Further miniaturization is possible but has to take into account the latter limitation. Carrier scattering under high field transport conditions results in a significant energy loss in the form of Joule heat which the device must be able to dissipate. If the device becomes too small and electric fields become large, the danger of device overheating is inevitable and care must be taken that the appropriate scaling rules are observed.

The transistor is one of the major components in information processing systems. By far, the transistor that has been utilized and still continues to play a leading role is the silicon based MOSFET which relies on transport at the quasi two-dimensional electron layer formed

between the oxide and the semiconductor. However, the effective mass of electrons in silicon is relatively large, approximately $0.19m_e$ where m_e is the free electron mass. In addition, the oxide-semiconductor surface exhibits a large degree of surface roughness scattering which, when coupled with interface charge scattering, results in considerably reduced mobilities compared to the bulk. It was recognized in the middle to late 1970s that a similar two dimensional electron gas could be formed in other systems such as at a semicoductor/semiconductor heterojunction or at a metal/semiconductor heterojunction with enhanced mobilities[1,2]. At around the same time reports were made of the observation of a high mobility two-dimensional electron gas at a GaAs/AlGaAs heterojunction[3]. GaAs has long been considered an attractive material for high speed device applications due to the low carrier effective mass and high peak electron velocity compared to silicon. The extremely high mobilities observed in GaAs/AlGaAs heterostructures are due to the technique of modulation doping in which the ionized donors are spatially separated from the two-dimensional electron gas. This technique was first suggested by Esaki and Tsu in 1969[5] and has since been perfected to result in greatly enhanced two-dimensional electron mobilities in excess of 10^6 $cm^2/V\text{-}s$ at low temperatures. As early as 1980 transistors based on these III-V compounds had been developed and showed promise as the technology of the future.[4] This technology has been advanced primarily from improvements in epitaxial growth techniques such as Molecular Beam Epitaxy (MBE) and Metallo-Organic Chemical Vapor Deposition (MOCVD), which allows for the growth of heterolayers with extremely sharp interfaces and thicknesses on the order of a few angstroms.

The GaAs/AlGaAs heterojunction is by far the most widely studied,

partly because of the less stringent conditions on its growth that emanates largely from the fact that the two compounds are almost lattice matched. The need for lattice matching is important for maintenance of high crystal quality, a major prerequisite in high performance devices. Recently it has been demonstrated that high crystal quality can be achieved without the need for lattice matching provided that one of the compounds comprising the heterojunction is grown thinner than some critical limit for misfit dislocations[6-12]. In such cases, the lattice mismatch is entirely accomodated by elastic strain resulting in very high quality materials. With the refined growth techniques mentioned above, achieving these growth standards is no longer a limitation and the field has become open to growth of heterojunctions of practically any kind, depending on the desired properties.

Among the systems that have drawn a great deal of attention has been the InGaAs/AlGaAs heterojunction. This system has many attractive properties which make it potentially superior to the aforementioned and much more widely studied GaAs/AlGaAs system in device performance. Some of these qualities are:

1. The InGaAs channel has both higher saturation and peak electron velocity than GaAs.
2. The InGaAs/AlGaAs system has a larger conduction band offset reducing the need for high Aluminum mole fractions believed to be responsible for the so called Persistent Photoconductivity effect (PPC).
3. It can be doped to much higher levels than the GaAs/AlGaAs system making it suitable for high current field effect transistors.
4. The InGaAs electrons have an effective mass of approximately

$0.050m_e$ compared to $0.067m_e$ for GaAs.

This latter advantage should make the InGaAs/AlGaAs system have much higher mobilities than the GaAs/AlGaAs system, but as will be discussed shortly, transport in the InGaAs channel has failed to yield mobilities that rival those of GaAs. This discrepancy has been explained by alloy scattering, which is a result of the random arrangement of Indium or Gallium on group III lattice site in Zinc-blende crystals and is thought to prevail in the InGaAs channel. This matter will be taken up in chapter 2 at a much more detailed level.

The purpose of the present work is to characterize the transport properties of InGaAs/AlGaAs heterojunctions. Two samples were studied, one grown and processed using the facilities of the Oregon State University Materials Research Laboratory and the other obtained from TriQuint Semiconductor, Beaverton, Oregon. Mobilities and carrier concentrations were measured and plotted as functions of temperature from 1.7 °K to 300 °K. Appropriate theories based on the scattering mechanisms in the channel were used to derive theoretical mobility versus temperature curves and the results compared with experiment. Measurements of Shubnikov de Haas oscillations at low temperatures allowed for the determination of the carrier effective mass from the temperature dependence of the oscillations amplitudes.

The organization of the paper is as follows: Chapter 2 presents an outline of the theoretical basis that underlies the behavior of quasi two-dimensional systems in semiconductors. Among the areas of major discussion are a detailed treatment of the various scattering mechanisms and the mechanisms of charge transfer and confinement. Also presented in this chapter is a literature review on the general present state of

transport in III-V compound heterojunctions with emphasis on the InGaAs/AlGaAs system. The experimental method is described in chapter 3 followed by a presentation of results in chapter 4. An analysis of the results based on the theory outlined in chapter 2 constitutes chapter 5 and chapter 6 summarises the findings.

II. THEORY AND REVIEW

The dynamics of electron transport in two dimensions is markedly different from that in three dimensions. Quantum mechanically, the envelope function describing an electron in a purely two dimensional system must be confined to a plane. In a real semiconductor the system cannot be regarded as two dimensional in the strict sense of the terminology, as the electron wave function has a finite spatial extent in the third dimension. In addition, electromagnetic fields cannot be confined to a plane and it is, therefore, more appropriate to refer to the system at hand as quasi two-dimensional. This means that the motion of the electron is free in the two dimensional plane but is restricted, or quantized in the third dimension. If the third dimension is called the z-direction, the energy levels are given by[13]

$$E = E_n + \frac{\hbar^2}{2m}(k_x^2 + k_y^2) \qquad (2.1)$$

where K_x and K_y are the wave vector components for motion parallel to the surface and the E_n are the electric quantum levels arising from confinement in the narrow potential well. The mechanism of confinement is described in the next section. Each value of E_n is the bottom of a two dimensional continuum called a subband. The calculation of the energy levels and wavefunctions depends on the nature of the subbands. The effective mass approximation is best suited for parabolic bands. In cases where the bands are non-parabolic, as is the case with Indium Arsenide, the **k.p** theory is appropriate. InGaAs subbands are not exactly parabolic, but the theory of transport will be developed under the

assumption of parabolicity for simplicity. The errors introduced by this approximation will be addressed in the analysis chapter.

The nature of the heterojunction is similar to that of a surface and electron transport is subject to all relevant surface scattering mechanisms, namely: interface charges and surface roughness scattering. In addition, transport in the present system is subject to alloy, remote impurity, background impurity, and acoustic phonon scattering. Because of the polar nature of III-V compounds, polar optical phonon scattering is also considered.

The chapter begins with a qualitative description of the mechanism of charge transfer and confinement in two dimensions before proceeding to discuss the various scattering mechanisms mentioned above. Transport in magnetic fields is then discussed in the context of the Hall effect and magnetoconductance and, finally, the chapter ends with a review of previous transport studies on III-V compound surface layers.

II.1 CHARGE TRANSFER AND CONFINEMENT

The structures of the present study are depicted in Figures 2.1 and 2.2. The InGaAs layer is shown sandwiched between GaAs and AlGaAs, all of which have a higher bandgap than the former. When two semiconductors of different bandgaps are grown, one on top of the other, the difference in the two bandgaps is taken up partially at the conduction band edge and partially at the valence band edge. In the present study, interest is in this behavior at the InGaAs/AlGaAs heterojunction. Figure 2.3a and 2.3b show the relative energy band diagrams of the two materials before and

GaAs		200 A
AlGaAs, Si–Doped 1E18		350 A
AlGaAs, Undoped		35 A
InGaAs, Undoped	(15% In)	150 A
GaAs, Undoped		1000 A
S.I. GaAs		

Figure 2.1 Layer structure of sample (S-1).

GaAs				300 A
AlGaAs	25% Al		(1E+17)	100 A
AlGaAs	25% Al		(1E+18)	100 A
GaAs			(2E+18)	100 A
AlGaAs	25% Al		(5E+16)	150 A
AlGaAs	Donor	25% Al	(2E+18)	200 A
AlGaAs	Spacer	25% Al		30 A
InGaAs	Channel	25% In		100 A
GaAs	Buffer			5000 A

Figure 2.2 Layer structure of sample (S-2).

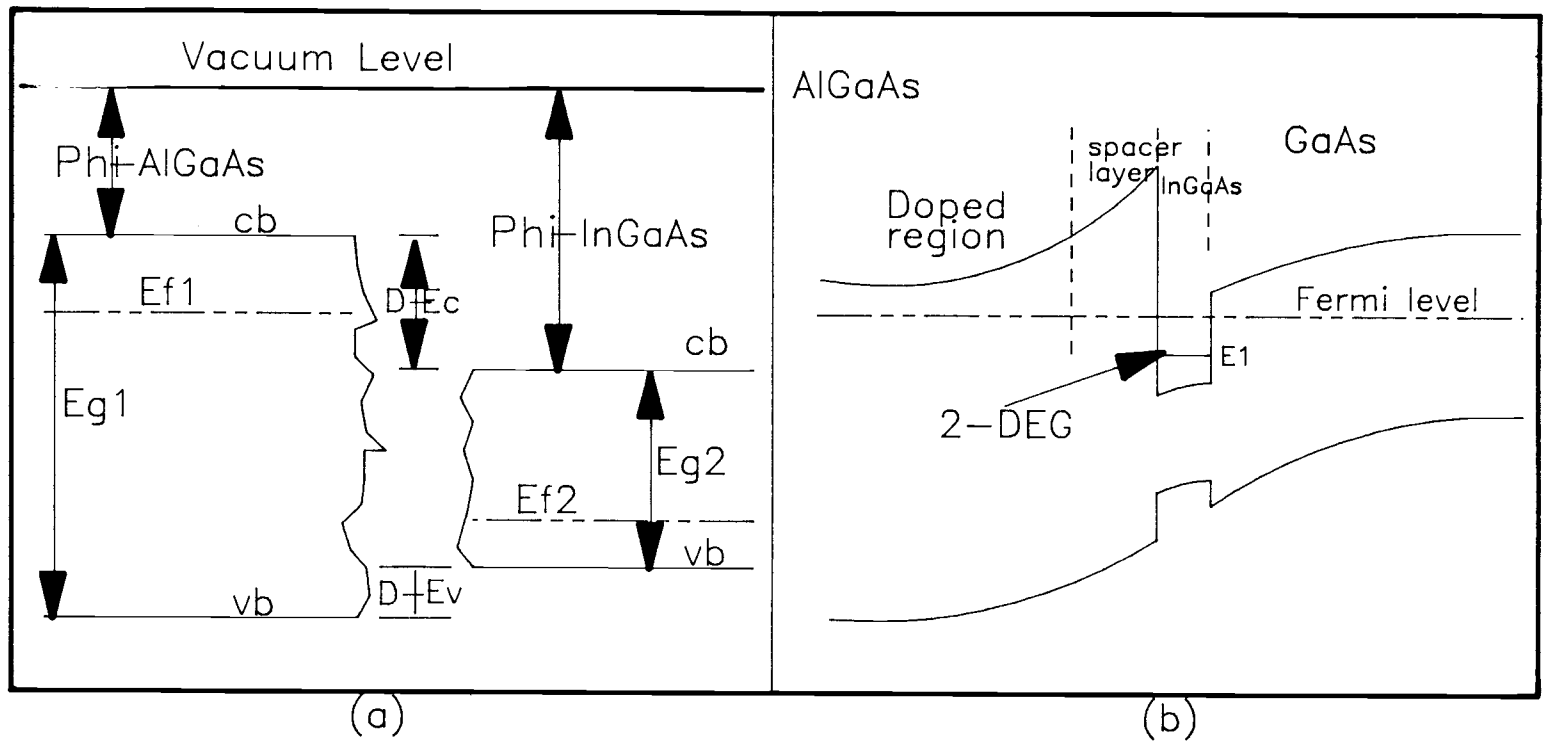

Figure 2.3 Energy band diagram before, (a), and after, (b), contact.

after contact. Figure 2.3b is based on the model by Anderson[61] which predicts that the conduction band offset will be given by the difference between the electron affinities of the two materials. A scale up of the top part of Figure 2.3b appears as Figure 2.4.

The position of the Fermi level depends on the number of electrons available in a material. When the two materials are brought into contact, thermodynamic equilibrium requires that the Fermi energy be constant across the junction. This results in electron transfer from the doped to the undoped side, thus raising the Fermi level on the latter side. This process continues until the fermi levels are the same. As charge is transferred, an electric field is created between the ionized donors and the transferred charge resulting in carrier confinement in a narrow well in the vicinity of the interface. As more charge is transferred, the electric field, and hence the potential, increases giving rise to more confinement. The degree of carrier confinement is, therefore, determined by the conduction band discontinuity and the position of the Fermi level in the undoped side relative to the doped side. It is this confined layer of electrons that is referred to as the quasi two- dimensional electron gas. A result of the two dimensional confinement is the formation of discrete energy levels in the direction of growth called subbands. In the description of quantization to follow, the quantum well will be approximated by a triangular well rather than a square well. The effects introduced by using a square well, especially on the variational parameter, are discussed in the next section.

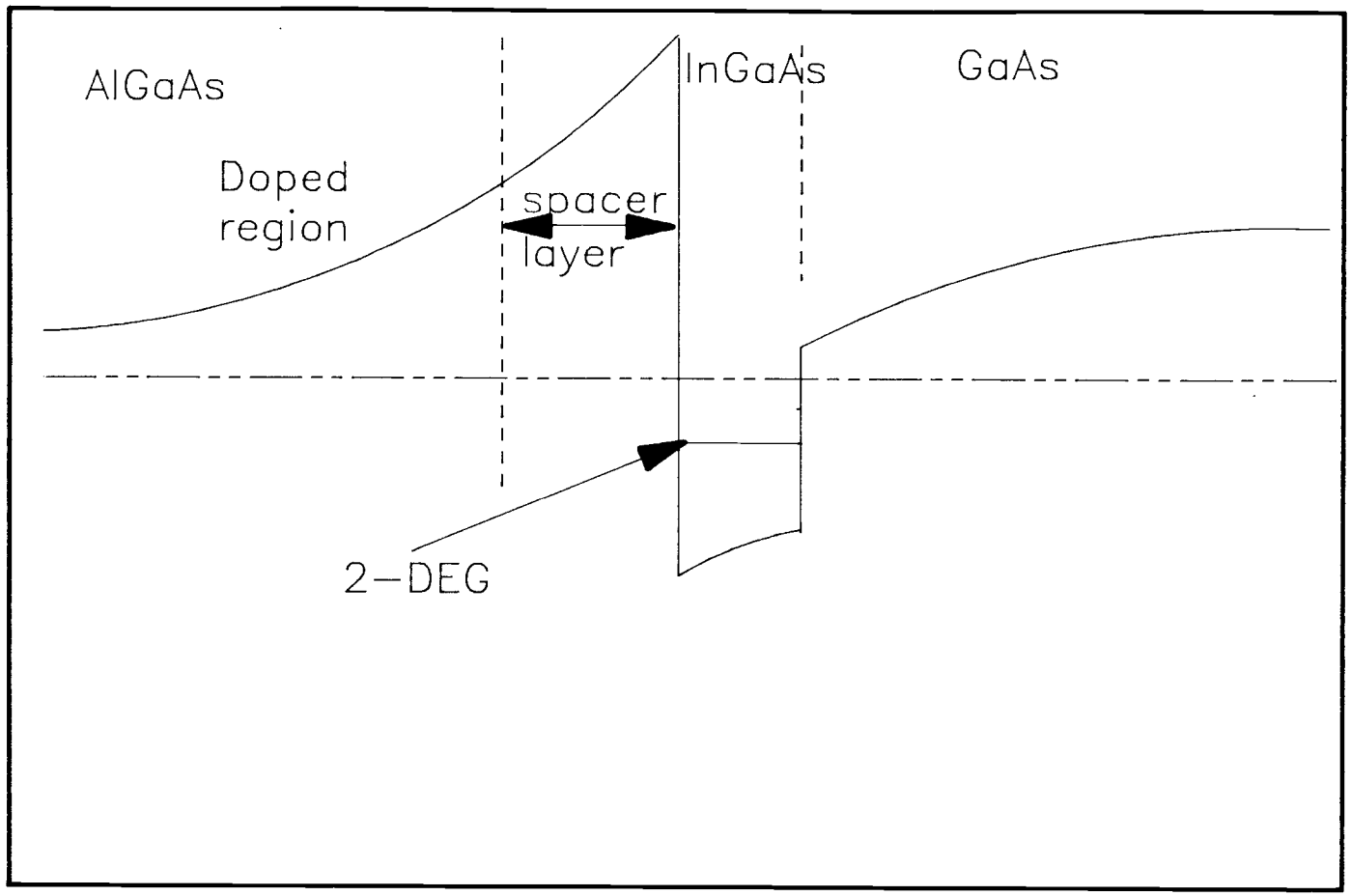

Figure 2.4 Conduction band profile of AlGaAs/InGaAs heterojunction.

II.2 QUANTIZATION

The effective mass approximation has been found to be sufficient in describing the effect of the surface potential in the formation of quantized states. In this approximation for a single band, the wave function of a heterojunction electron is written as a product of the Bloch function of that band, $e^{iK.R}U_K(R)$, and an envelope function $\Psi(R)$. $\Psi(R)$ satisfies the effective mass equation[13]

$$\left(-\frac{\hbar^2}{2m^*} + V(z) - E\right) \Psi(R) = 0 \tag{2.2}$$

where m^* is the isotropic effective mass perpendicular to the surface for the band considered and $V(z)$ is the surface potential.

If the potential in (2.2) is assumed to depend solely on the z-direction then the solution is separable as

$$\Psi(R) = \zeta_i(z)e^{i\mathbf{k}.\mathbf{r}} \tag{2.3}$$

where $\mathbf{k}$ and $\mathbf{r}$ represent the two dimensional wave vector and position vector in the plane parallel to the surface and $\zeta_i(z)$ is an envelope function satisfying[13]

$$\left(-\frac{\hbar^2}{2m_z^*}\frac{d^2}{dz^2} + V(z)\right) \zeta_i(z) = E_i\zeta_i(z) \tag{2.4}$$

The eigenvalues of (2.4) are given by

$$E_k = E_i + \frac{\hbar^2k^2}{2m^*} \tag{2.5}$$

These form a ladder of parabolic, two dimensional subbands where m^* is the mass parallel to the surface. The density of states for a two dimensional electron gas for parabolic bands is constant in energy, each subband contributing a constant density of states, such that the total density of states takes the form

$$D(E) = \sum_{i=0} \frac{n_v n_s m^*}{2\pi\hbar^2} \theta(E - E_i) \tag{2.6}$$

where n_v and n_s are the valley and spin degeneracies, respectively, and $\theta(x)$ is a step function. In the present case there is no valley and the spin degeneracy is 2 so that the density of states may be written as

$$D(E) = \sum_{i=0} \frac{m^*}{\pi\hbar^2} \theta(E - E_i) \tag{2.7}$$

It is assumed in this work that only the lowest subband is occupied. (2.4) may thus be re-written as

$$\left(\frac{\hbar^2}{2m_z^*} \frac{d^2}{dz^2} + V(z)\right) \zeta_0(z) = E_0 \zeta_0(z) \tag{2.8}$$

Analytic solutions to (2.8) have been found through the use of variational wave functions. The form of the variational solution most used is due to Fang and Howard[17] who considered an exponential function for the lowest subband.

$$\zeta_0(z) = \left(\frac{b^3}{2}\right)^{1/2} z e^{-bz/2} \tag{2.9}$$

Here b is the variational parameter found by minimizing the one electron

energy and has been calculated as[13]

$$b = \frac{12m_z^* e^2[N_{dep} + (11/32)\ N_s]^{1/3}}{\varepsilon_{channel}\hbar^2} \tag{2.10}$$

If corrections introduced by treating the quantum well as rectangular rather than triangular are introduced, the one electron ground state energy can be written as

$$E_0 = \frac{\hbar^2 b^2}{8m^*} + \frac{3e^2 N_{dep}}{\varepsilon_{channel} b} + \frac{33e^2 N_s}{32\varepsilon_{channel} b} + \left(\frac{Z_w^2 b^2}{2} + Z_w b + 1\right)e^{-Z_w}\ \Delta E_c \tag{2.11}$$

where Z_w is the well width and ΔE_c is the InGaAs/GaAs conduction band discontinuity. The new value of b is obtained by minimizing (2.11) with respect to b and numerically solving the resulting expression for b. Results obtained for $N_s = 1\times10^{12}/cm^2$ and $N_{dep} = 4.35\times10^{16}/cm^2$ are 4.8813×10^8 and 4.8242×10^8 for the triangular well and square well approximations, respectively. The difference is small but is significant, especially in mobility calculations. In the calculation of theoretical mobilities discussed in the next section, the latter value of b is used as its calculation more reflects the structure of the present study.

II.3 SCATTERING MECHANISMS

As mentioned earlier the treatment of transport in the present work will be discussed in the electric quantum limit ie. under the assumption that only the lowest subband is occupied. The complications of intersubband scattering are thus avoided and the mobility is determined

from an average over the distribution function evaluated in the relaxation time approximation. The assumption of the electric quantum limit may be far fetched for the present low mass samples, especially at 300 °K where carrier concentration is greatly increased.

II.3.1 Coulomb Scattering

Coulomb scattering at a heterojunction has contributions from ionized donor impurities located in the doped region, from background impurities, and from the charged states at the heterojunction which result from disorder associated with defects and impurities in the vicinity of the interface.

The main purpose of modulation doping is to reduce the influence of ionized donor impurity scattering by spatially separating the channel electrons from their parent donors. The large electron concentration of the channel further reduces scattering due to these impurities by screening. Despite these reductions, remote impurity scattering is still believed to play some role in influencing transport in the channel region and is included in the discussion

The general form of the relaxation time for Coulomb scattering is[13]

$$\frac{1}{\tau(k)} = \frac{2\pi}{\hbar} \sum_{k'} \int_{-\infty}^{\infty} N_i(z)dz \; |v_q(z)|^2(1-\cos\theta_{kk'}) \; \delta(E_k-E_{k'}) \qquad (2.12)$$

In (2.12) V_q is the two dimensional Fourier transform of the effective potential for electrons in the heterojunction and $N_i(z)$ is the concentration of either the charged centers at the interface, the remote impurity concentration, or background impurity concentration. V_q is given by[13]

$$V(q) = \frac{e^2}{2\epsilon_q} F(q,z_i) \tag{2.13}$$

where

$$F(q,z_i) = e^{qz_i} \int_0^\infty dz e^{-qz} |\zeta_0(z)|^2 \tag{2.14}$$

$$= \frac{b^3}{(b+q)^3} e^{qz_i}$$

Substituting (2.13) and (2.14) into (2.12), one obtains

$$\frac{1}{\tau(k)} = \frac{2\pi}{\hbar} \sum_{k'} \left(\frac{e^2 b^3}{2\bar{\epsilon} q (b+q)^3}\right)^2 (1-\cos\theta)\delta(E_k - E_{k'}) \times \int_{-\infty}^{\infty} N_i(z) e^{2qz_i} dz_i \tag{2.15}$$

For remote impurity scattering, the integral has meaning only in the depletion region in the doped AlGaAs layer, assuming that the spacer layer is free of impurities. Thus for remote impurity scattering, the integrand is evaluated from $-t_a$ to $-t_s$ where the former limit is the distance from the interface to the end of the doped region and t_s is the spacer layer thickness. The relaxation time becomes

$$\frac{1}{\tau_{ri}(k)} = \frac{m^* e^4 b^6}{8\pi\hbar^3\bar{\epsilon}^2} \int_0^{2\pi} d\theta \, A^2(q) \, N(q)(1-\cos\theta) \tag{2.16}$$

where

$$N(q) = \frac{N_D}{2q} \left(e^{-2qt_s} - e^{-2qt_a}\right) \tag{2.17}$$

and

$$A(q) = \frac{1}{q\varepsilon(q)(b+q)^3} \tag{2.18}$$

In carrying out the calculation for the relaxation time , it is assumed that all the donors are ionized so that N_D is just the AlGaAs doping

level. $\varepsilon(q)$ appearing in (2.18) is a term that accounts for screening and is given by

$$\varepsilon(q) = 1 + \frac{q_0}{q} F(q)\, \Pi(q) \tag{2.19}$$

Here q_0 is the inverse screening length and $F(q)$ is a slowly varying function on the order of unity that takes into account the broadening of the heterojunction from an ideal two-dimensional gas. $\Pi(q)$ is the wave vector dependence of the static polarization which, for finite temperatures, is given by[13,16]

$$\Pi(q;T,\mu) = \int_0^\infty \frac{\Pi(q;0,\mu)}{4k_BT\cosh^2\left(\frac{\mu-\mu'}{2k_BT}\right)}\, d\mu' \tag{2.20}$$

$\Pi(q;0,\mu)$ is the absolute zero expression for $\Pi(q;T,\mu)$

$$\Pi(q;0,\mu) = 1 - \theta(q-2k_F)\left[1 - \left(\frac{2k_F}{q}\right)^2\right]^{1/2} \tag{2.21}$$

The relaxation time for scattering by interface charges is determined in an identical manner as for remote impurities except that the integral appearing in (2.15) is evaluated under the assumption that the charges are uniformly distributed in the plane forming the interface. The relaxation time is then expressed as

$$\frac{1}{\tau_i(k)} = \frac{e^4 m^* N_i}{8\pi\hbar^3\bar{\varepsilon}^2} \int_0^\infty \frac{d\theta(1-\cos\theta)\, H^2(q)}{[q+q_0F(q)\Pi(q)]^2} \tag{2.22}$$

where $$H(q) = \int_0^\infty dz\, e^{-qz}\left|\zeta_0(z)\right|^2$$

and the rest of the quantities are as described for remote impurity scattering.

The calculation of the relaxation time for background impurity scattering is a little different. Here the integral appearing in (2.15) is evaluated from 0 to Z_w where Z_w is the well width. For $z_i>0$, $F(q,z_i)$ appearing in (2.14) is given by[13]

$$F(q,z_i) = \frac{1}{2}\left[1 + \frac{\varepsilon_{barrier}}{\varepsilon_{channel}}\right] P(z_i) + \frac{1}{2}\left[1 - \frac{\varepsilon_{barrier}}{\varepsilon_{channel}}\right] P_0 e^{-qz_i} \qquad (2.23)$$

where $$P_0 = \frac{b^3}{(b+q)^3} \qquad (2.24)$$

and $$P(z) = \frac{1}{8}\left[1 + 2bz + 2b^2z^2 + \frac{4}{3}b^3z^3\right] e^{-bz}, \quad q=b \qquad (2.25a)$$

For $q\neq b$, $$P(z) = \frac{b^3}{(b-q)^3}\left[e^{-qz} - (a_0 + a_1z + a_2z^2)\, e^{-bz}\right] \qquad (2.25b)$$

where $$a_0 = 2q\,\frac{(3b^2+q^2)}{(b+q)^3}$$

$$a_1 = \frac{4bq(b-q)}{(b+q)^2}$$

$$a_2 = \frac{q(b-q)^2}{(b+q)}$$

The rest of the calculation is similar to the remote impurity case.

II.3.2 Surface Roughness Scattering

Scattering by surface roughness has to be taken into account when discussing transport at heterojunctions unless the interface is truly

abrupt. One of the difficulties in the growth of the sample of the present study is the problem of Indium out-diffusion. The out-diffused Indium accumulates at the surface in a random fashion adding to the already random nature of the local atomic environment along the interface. When these are coupled with the surface potential, there results fluctuations in the subband energy giving rise to a finite lifetime in a given momentum state.

Present surface roughness models treat the displacement of the interface from a perfect plane as characterized by a random function $\Delta(\mathbf{r})$, $\mathbf{r}$ being the two dimensional position vector parallel to the surface. It is assumed that $\Delta(\mathbf{r})$ changes slowly over atomic dimensions such that the boundary may be treated as continuous and abrupt. Figure 2.5 is a schematic idealization of this function and it shows it as characterized by a mean height, Δ, and an average distance between bumps on the surface, L. The scattering potential is obtained by expanding the surface potential in terms of Δ as[13,16]

$$V_{SR}^{0} = V(z + \Delta(\mathbf{r})) - V(z) = \Delta(\mathbf{r})eF(z) + \cdots \qquad (2.26)$$

where F(z) is the electric field in the channel.

If corrections due to normal displacements of charge carriers from the surface as well as an electric field modification caused by a rough interface are taken into account[13]

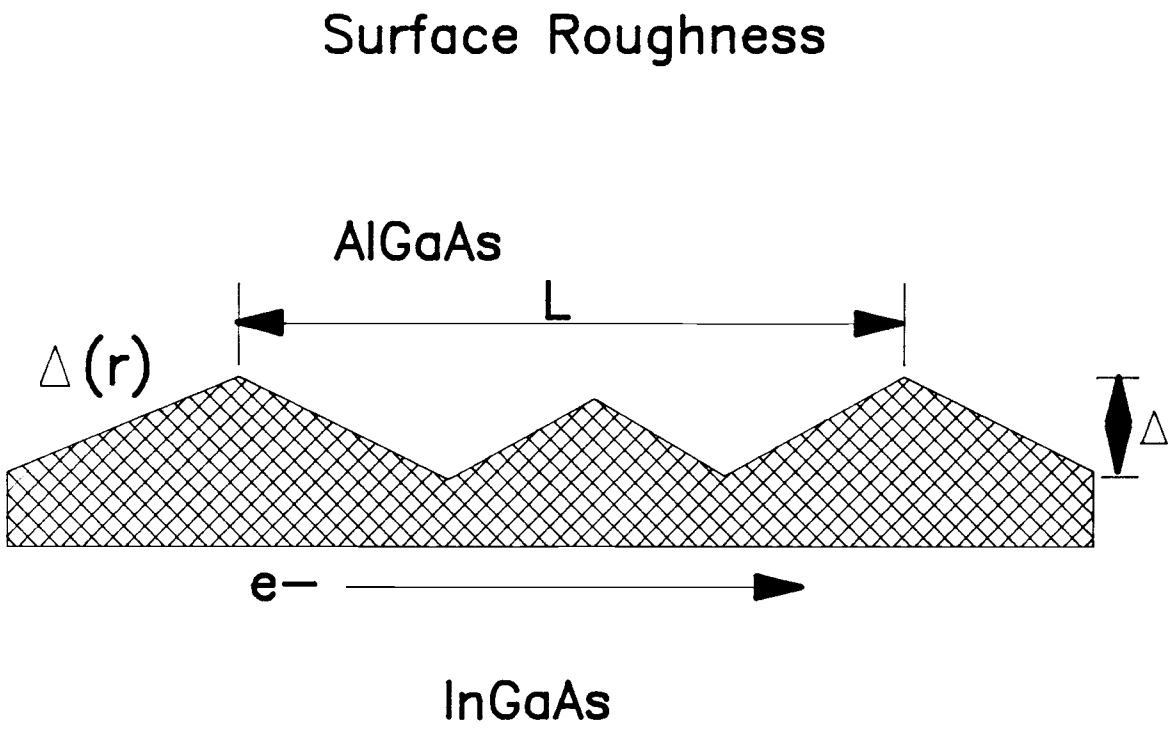

Figure 2.5 Idealized representation of surface roughness. Δ and L represent the rms height and Gaussian correlation length, respectively.

$$V'_{SR}(r,z) = e^2 \int d^2r'(z)dz'n(z'+\Delta(r))\ G(r,r';z,z') + \int_{S'} d^2r'(z)\left[G\frac{\partial V(z')}{\partial z'} - V(z')\frac{\partial G}{\partial z'}\right] - V(z) \qquad (2.27)$$

arises where n(z) is the carrier density $N_s\zeta_0^*(z)\zeta_0(z)$, V(z) is the unperturbed surface potential in the InGaAs channel, G is the electrostatic Green's function transform given by[16]

$$G(q,z-z') = \frac{1}{2q\varepsilon_{channel}}\left[e^{-q(z-z')} + \alpha e^{-q(z+z'+)}\right] \quad z'>0$$
$$= \frac{1}{2q\varepsilon} e^{-q(z-z')} \quad z'<0 \qquad (2.28)$$

The scattering matrix element calculated using only first order terms in Δ_q and making use of convolution is

$$\langle k|V_{SR}|k'\rangle = \Delta_q \int_0^\infty dz\ |\zeta_0(z)|^2 \{e^2N_s \int_0^\infty dz'G(q,z-z')\frac{\partial}{\partial z'}|\zeta_0(z)|^2 + eF_s\left(\frac{\partial G(q,z-z')}{\partial z'} - \frac{\partial G(q,z-z')}{\partial z}\right)\Big|_{z'=0}\} \qquad (2.29)$$

where $G(q,(z-z'))$ is given by (2.28) for $z'>0$. The scattering rate for a single subband in the Born approximation becomes

$$\frac{1}{\tau_{SR}} = \Delta^2L^2e^4\left(N_{dep} + \frac{1}{2}N_s\right)^2 m^* \int_0^{2\pi} d\theta(1-\cos\theta)e^{-k^2L^2\sin^2(\theta/2)} \times \left[\frac{\Gamma(2k\sin(\theta/2))}{\varepsilon(2k\sin(\theta/2))}\right]^2 \qquad (2.30)$$

where Δ represents the root mean square height of the surface roughness, L is the correlation length (see Figure 2.5), $\varepsilon(2k\sin(\theta/2))$ is the

dielectric function and $\Gamma(x)$ is a correction term on the order of unity.

II.3.3 Acoustic Phonon Scattering

For small phonon wave vectors the deformation potential concept may be applied to the acoustic interaction. This concept is based on the assumption that the interaction of electrons with long wave-length acoustic mode is equivalent to the effect of a locally homogeneous strain. The acoustic scattering rate calculated in this aproximation is[16,62-64]

$$\frac{1}{\tau_{ac}} = \frac{\lambda m^* \Xi_1^2 k_B T}{\hbar^3 \rho_m V_s^2 W_j} \tag{2.31}$$

where Ξ is the deformation potential, V_s is the velocity of sound, ρ_m is the density of the material, w_j is the channel thickness, and λ is an overlap integral of order unity.

II.3.4 Polar Optical Phonon Scattering

The bonding in compound semiconductors is partially ionic resulting in a polarization field arising from the coulomb interaction between the different effective charges residing in non-equivalent lattice sites. The polarization field arising from the typical longitudinal-optical mode causes a polar-optical interaction with the channel electrons. The matrix element for this interaction is found by first treating the lattice as a continuum characterized by its polarization $\mathbf{P}(\mathbf{r})$ at the point $\mathbf{r}$. The momentum relaxation time can be written as[51]

$$\frac{1}{\tau_{pop}} = \frac{eE_0}{2\hbar}\left[N_{wo}\int_0^{2\pi} d\theta \frac{H_{ij}(q^+)}{q^+}(1-\cos\theta) + (N_{wo}+1)\int_0^{2\pi} d\theta \frac{H_{ij}(q^-)}{q^-}(1-\cos\theta)\,\theta(E-\hbar w_{LO})\right] \tag{2.32}$$

where $$H_{ij}(q) = \int_{-\infty}^{\infty} dz \int_{-\infty}^{\infty} dz' \rho_{ij}^*(z)\rho_{ij}(z')e^{-q(z-z')} \tag{2.33}$$

and $$eE_0 = \frac{m^* e^2 \hbar w_0}{4\pi\hbar^2}\left[\frac{1}{\varepsilon_{00}} - \frac{1}{\varepsilon_0}\right] \tag{2.34}$$

Here ε_{00} and ε_0 are the high and low frequency dielectric constants, respectively. Using the variational wavefunction, (2.9), the density for the lowest subband is found[13]

$$\rho_{00}(z) = \frac{b^3}{2} z^2 e^{-bz} \tag{2.35}$$

and the scattering Hamiltonian becomes

$$H_{00}(q) = \int_0^{\infty} dz \int_0^{\infty} dz' \frac{b^3}{2} z^2 e^{-bz} \frac{b^3}{2} z'^2 e^{-bz'} e^{-b(z-z')}$$

$$= \left(1 + \frac{9}{8}\frac{q}{b} + \frac{3}{8}\frac{q^2}{b^2}\right)\left(1 + \frac{q}{b}\right)^{-3} \tag{2.36}$$

With the above, the momentum relaxation time is obtained as

$$\frac{1}{\tau_{pop}} = \frac{eE_0}{2\hbar}\left[N_{wo}\int_0^{2\pi} d\theta \frac{f(q^+)(1-\cos\theta)}{q^+} + (N_{wo}+1)\int_0^{2\pi} d\theta \frac{f(q^-)(1-\cos\theta)}{q^-}\theta(E-\hbar w_0)\right], \tag{2.37}$$

Here $$N_{wo} = \frac{1}{(e^{\hbar w_0/kT} - 1)} \tag{2.38}$$

$$f(q) = \left(1 + \frac{9}{8}\frac{q}{b} + \frac{3}{8}\frac{q^2}{b^2}\right)\left(1 + \frac{q}{b}\right)^{-3} \tag{2.39}$$

and $$q^{\pm} = \left[2k^2 \pm \frac{2w_0 m^*}{\hbar} - 2k\left(k^2 \pm \frac{2w_0 m^*}{\hbar}\right)^{1/2}\cos\theta\right]^{1/2} \qquad (2.40)$$

In (2.37), the first term corresponds to the absorption and the second to the emission of a phonon.

II.3.5 Alloy Scattering

It was mentioned earlier that no complete theory presently exists in the literature for the treatment of alloy scattering in semiconductor compounds. The points of uncertainty lie in the proper estimate of the scattering potential and the degree of randomness to be assumed in the calculations. Nevertheless, several authors[15,19,20-24] have formulated various theories and it has generally been concluded that in ternaries, alloy scattering is the dominant mechanism at low temperatures and, if impurity scattering is properly eliminated, a study of alloy scattering may lead to a correct estimate of alloy scattering potential.

A knowledge of the actual distribution of atoms in the alloy is necessary for the development of any theory of alloy scattering, the total scattering potential being a sum over all contributions due to all atoms or groups of atoms at the various alloy sites.

Consider an alloy of composition $A_xB_{1-x}C$. In the conventional theory of alloy scattering, the constituent type A and type B atoms pairs are assumed to be randomly distributed within the volume of the crystal.[47,48] In present models, the alloy cluster theory has mostly been used.[22-24] In this theory, clustering of group III atom pairs is assumed to take place, forming islands of type A or type B atom pairs. The choice of the potential at the alloy sites has not been uniform either. Ando and Bastard[20,21] used in their theories a delta function for the scattering

potential. This is reasonable for the conventional model but for the cluster theory, a better approximation is to assume a spherically symmetric square well potential.[24,49] In this work, the methods of Ref. 21 are adopted.

The procedure involves a self-consistent determination of the bound state wave functions of the channel which are then used to evaluate the momentum relaxation time and subsequently, the mobility limited by alloy scattering. The Schrodinger and Poisson equations are solved self-consistently by using a wave function that is a generalization of the usual Fang and Howard wavefunctions to take into account the penetration of the wave function into the barrier. In the electric quantum limit, these are[21]

$$\zeta_1(z) = \begin{cases} M_1 e^{k_1 z/2} & z < 0 \\ N_1 (z + z_0) e^{-b_1 z/2} & z > 0 \end{cases} \tag{2.41}$$

where k_1 and b_1 are variational parameters and all the other constants are determined by the continuity of ζ_1 and $\frac{1}{m(z)} \frac{\partial \zeta_1(z)}{\partial z}$ at the interface and by the condition

$$\int_{-\infty}^{\infty} |\zeta_1(z)|^2 \, dz = 1 . \tag{2.42}$$

k_1 is taken equal to $2(m^* V_b/\hbar^2)^2$ where V_b is the conduction band discontinuity.

Because the transport channel is a disordered alloy, the two-dimensional electrons are scattered by the short range fluctuating alloy potential. If $|E_1, k_{11}\rangle$ is the eigenstate corresponding to a free motion

with 2-D wave vector k_{11} in the layer plane and the z motion is described by ζ, the momentum relaxation time associated with alloy scattering is

$$\frac{1}{\tau_{all}} = \frac{2\pi}{\hbar} x(1-x) \frac{\Omega_0}{S} |\langle V_0 \rangle|^2 \int_0^{Z_w} dz\, \zeta_i^4(z) \sum_{k'} \delta(E_k - E_{k'}) \quad (2.43) \qquad (2.43)$$

assuming a perfectly random alloy. In the above, Ω_0 is the alloy unit cell, Z_w the quantum well width, S the sample area, x the Indium mole fraction in the alloy and $\langle V_o \rangle$ is the spatial average of the fluctuating alloy potential over the alloy unit cell obtained by fitting the low temperature mobility data[55]. $\langle V_o \rangle$ is therefore an adjustable parameter. The summation under the integral is the constant density of states per spin, $m^*S/2\pi\hbar^2$. The value of the integral evaluated, for simplicity, with $Z_w = \infty$ is[15] (3/16)b so that the relaxation time becomes

$$\frac{1}{\tau_{all}} = \frac{3}{16} m^* \frac{x(1-x)\, \Omega_0 \langle V_0 \rangle^2\, b}{\hbar^3} \qquad (2.44)$$

II.4 TRANSPORT IN MAGNETIC FIELDS

The magnetic field is a tool that is routinely used by physicists and engineers to probe the properties of materials. In the present work it is used to determine the transport properties of the two dimensional electron gas formed at the InGaAs/AlGaAs heterojunction. In fact the two-dimensional nature of a heterojunction electron gas is most accurately ascertained by observing the angular dependence of magnetoresistance. Shubnikov de Haas oscillations are only observed for fields perpendicular to the interface, vanishing altogether when the

field is applied parallel to the interface. From these oscillations, the effective mass of charge carriers can be determined. Hall measurements provide a direct way of determining both electron concentration of the transport channel as well as their mobility. The discussion to follow will treat transport in magnetic fields in the context of Hall effect and magnetoconductance, in each case presenting expressions for the relevant transport parameters.

II.4.1 The Hall Effect

Consider the two-dimensional structure of Figure 2.6. A constant current is maintained between points A and B and a magnetic field is applied in the z direction perpendicular to the surface.

The condition that current flows only in the x-direction requires that

$$\mathbf{eE} = e(\mathbf{V} \times \mathbf{B}) \tag{2.45}$$

where **E** is the Hall field, **V** is the electron drift velocity along the channel, **B** is the magnetic induction, and e is the charge of an electron. From Figure 2.6

$$\mathbf{V} \times \mathbf{B} = \begin{bmatrix} \hat{i} & \hat{j} & \hat{k} \\ V_x & 0 & 0 \\ 0 & 0 & 0 \end{bmatrix} = -\hat{j}\, V_x B_z \tag{2.46}$$

resulting in $E_y = -V_x B_z$ where $V_x = J_x/ne$

Thus, $$E_y = -J_x B_z / n_e \tag{2.47}$$

The Hall coefficient is defined such that $E_y = R_H J_x B_z$ so that $R_H = -1/ne$. More generally, however, the Hall coefficient is expressed

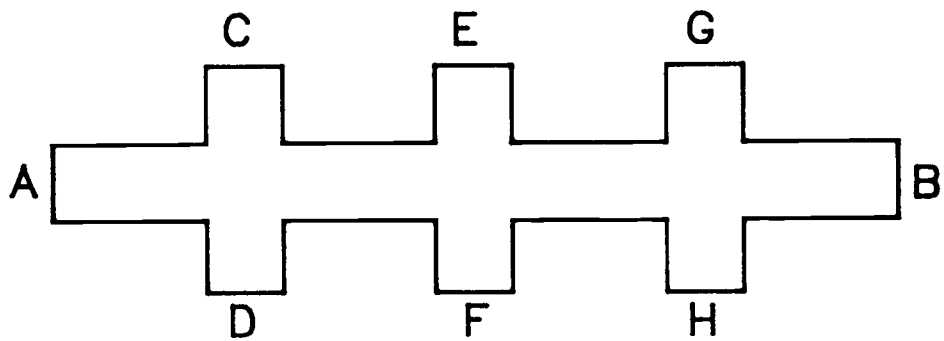

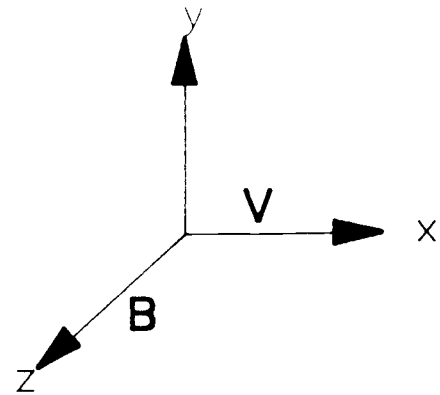

Figure 2.6 Hall structure geometry. **V** is the electron velocity and **B** is the magnetic induction.

as $R_H = -r/ne$ where r is called the Hall factor and depends on the scattering mechanisms through their average relaxation time

$$r = \frac{\langle \tau^2 \rangle}{\langle \tau \rangle^2} \tag{2.48}$$

This quantity is usually not too different from unity and will be assumed to be equal to one in this work. For electrons, $\sigma = ne\mu_e$ where $\mu_e = |R_H|\sigma$ is the electron mobility. From equations 2.45 to 2.47, the following important equations are obtained.

$$\sigma = \frac{I_x}{V_x}\frac{L_1}{L_2} \tag{2.49}$$

$$\mu = \frac{1}{B}\frac{V_H}{V_x}\frac{L_1}{L_2} \tag{2.50}$$

$$n = \frac{I_x B}{V_H e} \tag{2.51}$$

II.4.2 Magnetoconductance

A sufficiently high magnetic field applied perpendicular to the interface quantizes the motion of electrons parallel to the surface, resulting in the collapse of the two dimensional density of states into fully quantized Landau levels. This quantization is responsible for the magneto-oscillatory behavior for heterojunction electrons, the most notable of which is the Shubnikov de Haas (SdH) effect. For a fixed current along the channel, periodicity in 1/B of the conductivity is observed as the magnetic field is swept, the peaks occuring when the Fermi surface coincides with a given Landau level. For moderate fields,

SdH oscillations are nearly sinusoidal in 1/B, a result of, among other mechanisms, thermal broadening and scattering. At higher fields spin splitting occurs and the analysis of the oscillations becomes more complicated.

In the absence of spin splitting, the orbital motion of the channel electrons is quantized into harmonic oscillator-like states with energies

$$E = E_i + (n + 1/2)\hbar w_c \tag{2.52}$$

Here E_i is the bottom of the i^{th} subband, $w_c = eB/m^*$, and n is the Landau level quantum number, 0,1,2,3..... For a spherical conduction band minimum, the electrons follow circular paths in position space. The k-space trajectories are also circular with the area for such an orbit in the k_x, k_y plane given by

$$A = \left(\frac{2\pi eB_z}{\hbar}\right)\left(n + \frac{1}{2}\right) \tag{2.53}$$

From (2.5) and the density of states for a single subband, (2.6), the Fermi radius for a given subband is

$$k_F = \left(\frac{4\pi N_s}{n_s n_v}\right)^{1/2} \tag{2.54}$$

$$A_F = \frac{4\pi^2 N_s}{n_s n_v} \tag{2.55}$$

where A_F is the area enclosed by the Fermi surface, and n_S and n_V are as described earlier. A peak in the conductivity occurs when (2.53) and (2.55) are equal

$$\left(\frac{2\pi eB_z}{\hbar}\right)\left(n + \frac{1}{2}\right) = \frac{4\pi^2 N_s}{n_s n_v} \tag{2.56}$$

The spacing between successive Landau levels is thus periodic in 1/B and is given by

$$\Delta\left(\frac{1}{B_z}\right) = \frac{en_s n_v}{2\pi\hbar N_s} \tag{2.57}$$

A knowledge of the magnetic field inverse period thus allows for the determination of N_s, the channel electron concentration.

The smoothing out of the conductivity peaks by thermal broadening results in considerable amplitude reduction. As in the three-dimensional SdH effect, the temperature dependence of the oscillations amplitude can be written as[50]

$$A = \frac{2\pi^2 k_B T/\hbar w_c}{\sinh(2\pi^2 k_B T/\hbar w_c)} \tag{2.58}$$

where A is the amplitude of the oscillations. The cyclotron frequency, w_c, is related to the carrier effective mass through $w_c = eB/m^*$ and, therefore, by fitting the observed temperature dependence to the function, the effective mass can be extracted.

II.5 LITERATURE REVIEW

The accumulation of carriers at a heterojunction interface was first predicted by Anderson in 1960[14]. In 1969 Esaki and Tsu suggested that this should result in an enhanced carrier mobility due to separation of carriers from the ionized donors.[26] This mobility enhancement was first reported by Dingle et al. in 1978 on a GaAs/AlGaAs semiconductor

superlattice[27], with the first transistor based on this enhanced mobility structure being demonstrated only two years later.[4] The mobility values reported by Dingle and his group were 1.5×10^4 $cm^2/V\text{-}s$ below 50 °K and approximately 5,000 $cm^2/V\text{-}s$ at 300 °K and were a marked improvement over hitherto reported values for uniformly doped GaAs/AlGaAs structures, typically 1,000-2,500 $cm^2/V\text{-}s$ at room temperatures and not much different at lower temperatures.[27,28] The following years saw rapid improvements in mobility figures for the AlGaAs-GaAs heterostructure system that exceeded 1×10^6 $cm^2/V\text{-}s$ by 1983. These rapid improvements were a result of improved sample growth techniques utilizing, mostly, the refined techniques of MBE and MOCVD described earlier.

Studies of transport in modulation doped strained InGaAs structures, the materials of the present study, were much slower coming and did not start until late 1982 when Fritz et al.[29] succeeded in growing an InGaAs-GaAs strained layer superlattice. Prior to this, some transport studies had been carried out on InGaAs structures grown lattice-matched to InP. In these studies and subsequent ones, it was invariably observed that electron mobilities in the InGaAs channel were consistently lower than those in GaAs as measured for the GaAs-AlGaAs heterostructure at lower temperatures and around 10 to 30% higher at room temperature.[30] Table 2.1 summarizes these comparisons for the period between 1979 and 1985.

The late start in the study of strained modulation doped InGaAs structures can be attributed to the difficulty in achieving high quality growth materials as a result of the lattice mismatch which often results in the formation of dislocations. Improvements in the growth technology and the understanding of the origin of misfit dislocations and how to prevent them alleviated this problem. To date, a series of studies,

Table 2-1 A profile of two dimensional electron gas mobilities and concentrations of selectively doped heterostructures.

Material	Year	300 K	77 K (dark)		4.2 K (dark)		4.2 K (light)	
		Mobility ($cm^2/V \cdot s$)	Mobility ($cm^2/V \cdot s$)	Concen. (cm^{-2})	Mobility ($cm^2/V \cdot s$)	Concen. (cm^{-2})	Mobility ($cm^2/V \cdot s$)	Concen. (cm^{-2})
GaAs/N-AlGaAs (MBE)	1979				5,000	1.1×10^{12}		
	1980	4,600	28,600				25,500	1.0×10^{12}
		6,190	61,000	5.7×10^{11}				
	1981	7,450	74,200		115,000			
		8,030	117,000	4.9×10^{11}	244,000	4.9×10^{11}		
							365,000	1.1×10^{12}
	1982	8,720	122,000	5.6×10^{11}	256,000	5.5×10^{11}		
					218,000	5.5×10^{11}	396,000	1.1×10^{12}
			165,000	3.4×10^{11}	540,000	3.4×10^{11}	1,150,000	4.7×10^{11}
	1983		195,000	3.0×10^{11}	1,250,000	3.0×10^{11}	2,120,000	5.0×10^{11}
	1984	9,200	200,000	2.2×10^{11}	1,060,000	2.2×10^{11}	1,700,000	3.9×10^{11}
	1985		200,000	3.6×10^{11}	1,550,000	3.6×10^{11}	2,400,000	5.3×10^{11}
GaAs/N-AlGaAs (MOCVD)	1981		45,000	10^{12}				
	1982		100,000		160,000	5.0×10^{11}		
	1984		154,000	5.1×10^{11}	445,000	5.1×10^{11}	510,000	8.0×10^{11}
InGaAs/N-InAlAs (MBE) or InGaAs/N-InP (CVD)	1982	8,915	60,120		90,420 (10K)			
		10,000	68,000		93,000	7.1×10^{11}		
	1983	9,400	71,400		106,000	2.0×10^{11}		
	1985	11,000	56,000		70,000	$8-9 \times 10^{11}$		
			83,000					
		11,000	82,000	8.3×10^{11}	110,000	8.0×10^{11}		

mainly on Field Effect Transistor device performance have been carried out, principally by two groups at the University of Illinois, Urbana-Champagne and at Cornell University, Ithaca, New York.[31,36] The best reported transport measurements for this system are mobilities of 8,000; 95,000; and 158,000 $cm^2/V\text{-}s$ at 300; 77; and 10 °K, respectively for a 100 angstroms spacer layer thickness and a 2-dimensional concentration of 3×10^{11} cm^{-2}. The mobility values drop to 6,000 $cm^2/V\text{-}s$ and 29,000 $cm^2/V\text{-}s$ at 300 °K and 77 °K for a spacer layer thickness of 30 angstroms while concentrations increase to 1.4×10^{12} and 1.2×10^{12} cm^{-2}, respectively.[32]

Electrons in $In_xGa_{1-x}As$ have an effective mass that ranges from $0.023m_e$ to $0.067m_e$, the effective masses for electrons in InAs and GaAs, respectively, depending on the mole fraction, x, of Indium in the compound. These values are obtained by, among other methods, cyclotron resonance and from Shubnikov de Haas oscillations measurements.[37-41] The theory behind the Shubnikov de Haas method for the 3-D case was worked out by Lifshitz and Kosevich in 1956 and is discussed by Khalid, et al.[42] In this theory the temperature dependence of the oscillations amplitude is approximately given by (2.58). A knowledge of the amplitude as a fuction of temperature for a given field allows for the extraction of the effective mass. A few authors[42,43,52] have noticed an apparent increase in effective mass with magnetic field for mercury, bulk InAs, and 2-D GaAs electrons, respectively. This mass dependence on magnetic field has also been noticed in the present study and will be discussed in Chapter 5.

The mass dependence on x is approximately linear and, for x less than 0.5, which is usually the case, this mass is considerably lower than that of GaAs electrons. Much hope has been placed on this fact to result

in higher electron mobilities in InGaAs than GaAs. So far, however, this has only been a reality at high temperatures. A theory of alloy scattering has been proposed to account for the degraded low temperature mobilities and the results have generally supported the observations.[15,21,23,44-47] It has to be noted, however, that the theory of alloy scattering is not very well established and, infact, no single theory is presently available in the literature. There are two sources of uncertainty concerning the absolute magnitude of mobility limited by alloy scattering. One is the uncertainty in the degree of randomness of the alloy which is usually assumed to be total and the second is the lack of certainty in the appropriate value for the alloy scattering potential. This latter quantity is usually assigned a value of 0.6 eV, the bulk InGaAs scattering petential.[21] Until these approximations are verified the values of mobility limited by alloy scattering will also merely be approximations.

III. EXPERIMENTAL PROCEDURE

This study involved an investigation of the electron transport properties of InGaAs/AlGaAs heterojunctions on two samples. The experimental work performed falls into two categories: sample preparation and transport measurements. Sample (S-1) (Figure 3.1) was grown and processed using the facilities of the Oregon State University Materials Research Laboratory while sample (S-2) (Figure 3.2) was provided by TriQuint Semiconductor, Beaverton, Oregon. The available information on the growth and processing of the latter sample are presented at the end of section 3.1.

III.1 SAMPLE PREPARATION

Sample (S-1) was grown using a Perkin Elmer 42513 MBE system equipped with Scanning Auger Microscope (SAM), Reflection High Energy Electron Diffraction (RHEED) system and a Quadrupole Mass Spectrometer (QMS). The details of epitaxial film growth and the utility of the various mentioned tools in monitoring the growth process can be found in Ref.12. The lattice constant of GaAs is 5.653 Angstroms while that of $In_xGa_{1-x}As$ lies between 5.653 and 6.059 angstroms, the lattice constants of GaAs and InAs, respectively, the actual value depending on the mole fraction, x, of Indium in the ternary. Higher values of x shifts the lattice constant of InGaAs towards the upper limit and as a result, makes it further apart from that of GaAs, the layer on which it is grown. The lattice constant mismatch at the heterojunction results in biaxial

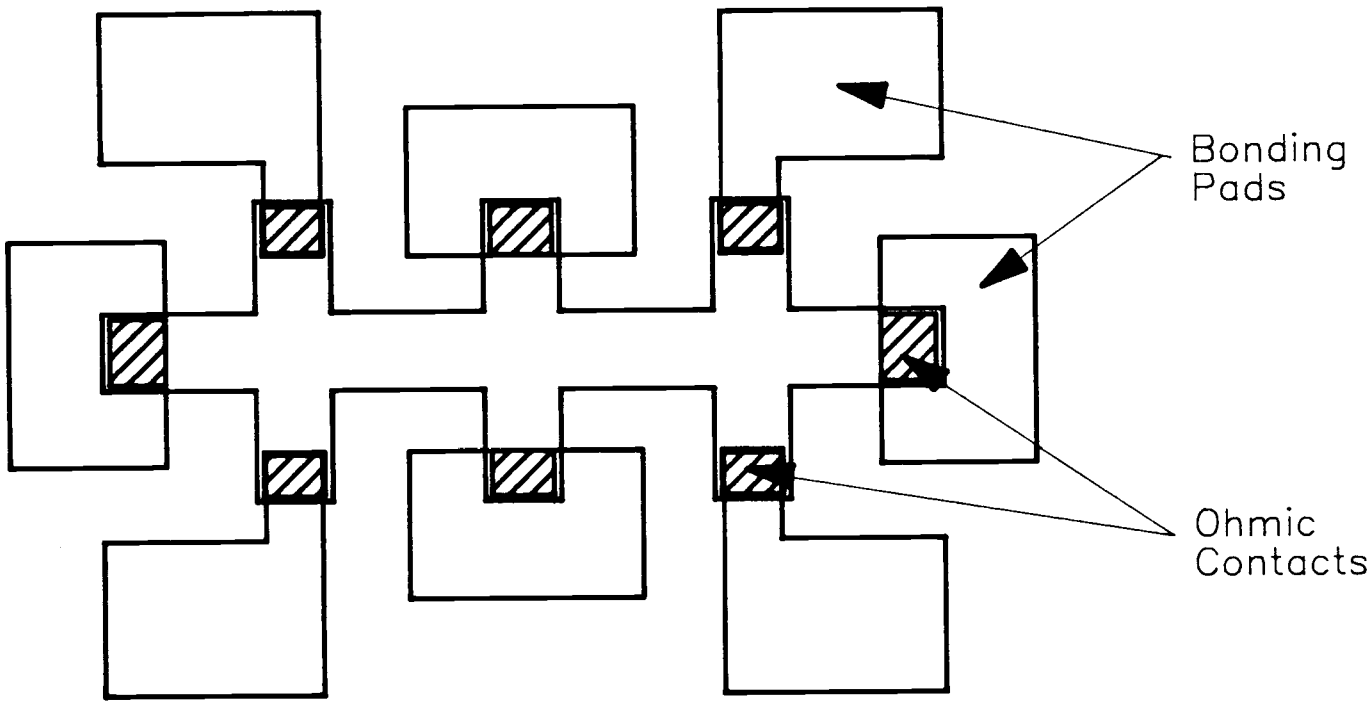

Figure 3.1 Hall structure showing ohmic contacts and bonding pads for sample (S-1).

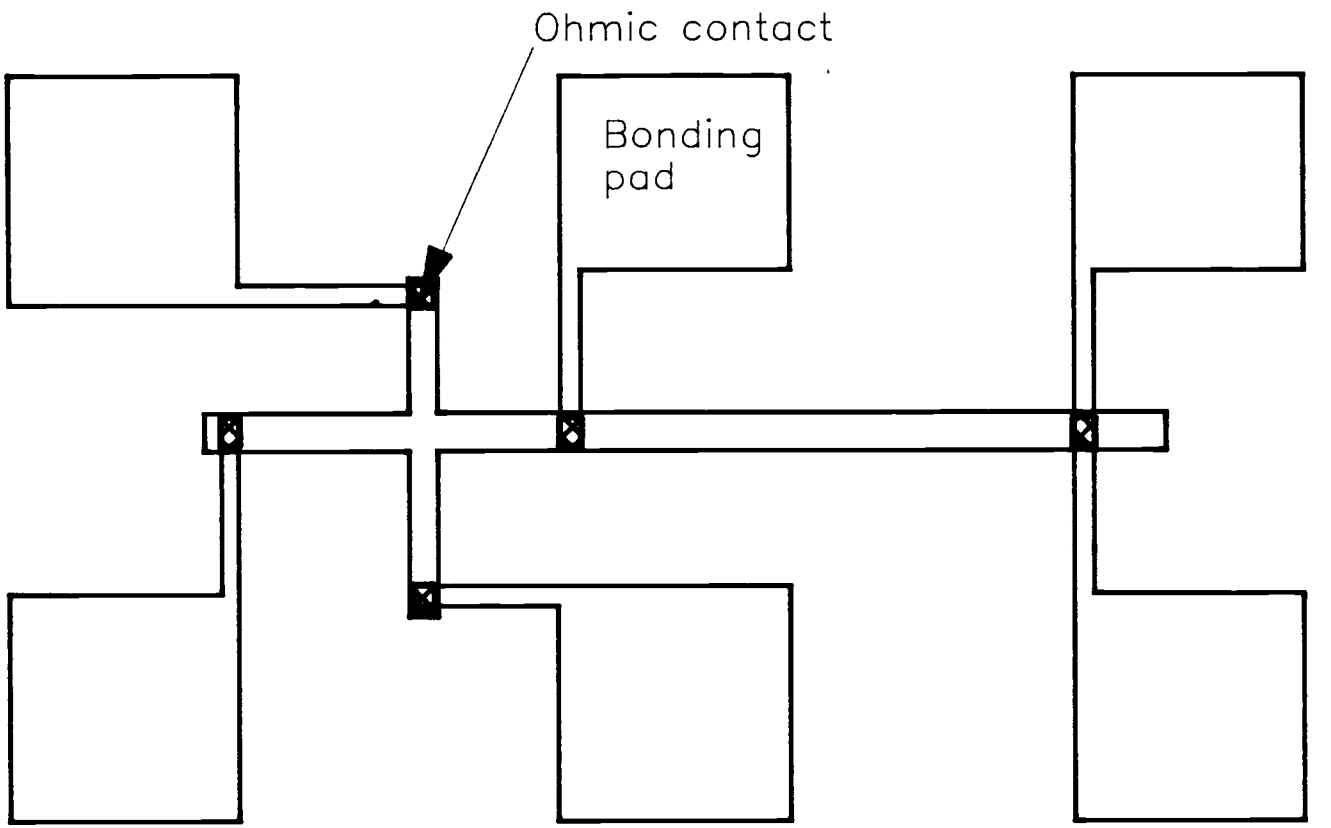

Figure 3.2 Hall structure showing ohmic contacts and bonding pads for sample (S-2).

compression for InGaAs and may result in dislocations if the strain gets too high. As mentioned in the introduction and in Chapter 2, dislocation free structures can be grown if the InGaAs layer does not exceed a critical thickness limit for dislocation formation (Figure 3.3). To find out the quality of the samples grown, photoluminescence (PL) measurements were made on the sample. From the ranges of optical transition energies it could be determined if the structure was dislocation free or not.

The resulting sample was subjected to two stages of photolithography, the final result of which is shown in Figure 3.1. Each stage was a two mask sequence that consisted of standard photolithography and lift off, in that order. The purpose of the first mask of the initial stage was to lay out the Hall geometry. The exposed sample was developed and then etched for twelve seconds in an H_2O_2:NH_4OH:H_2O solution in the volume ratio 1:1:5 to obtain Hall structure mesas on which the ohmic contacts were defined using the second mask set. The metal contacts were then evporated using a Veeco 7760 series metal evaporator. These consisted of a deposit of nickel followed by a gold-germanium eutectic alloy and then gold in the mass ratio 1:10:10, respectively. A silicon dioxide layer was then deposited on the sample using a Veeco Michrotech system before annealing the sample for five minutes at 450 °C.

The second stage was also divided into standard and lift off mask procedures, except that, now, the purpose was to break the oxide layer and lay out bonding pads, respectively. Another notable difference between the two stages is that a BHF etchant was used instead of the H_2O_2:NH_4OH:H_2O solution and the etchant was applied for forty five seconds instead of twelve. The bonding pads consisted of a deposit of titanium

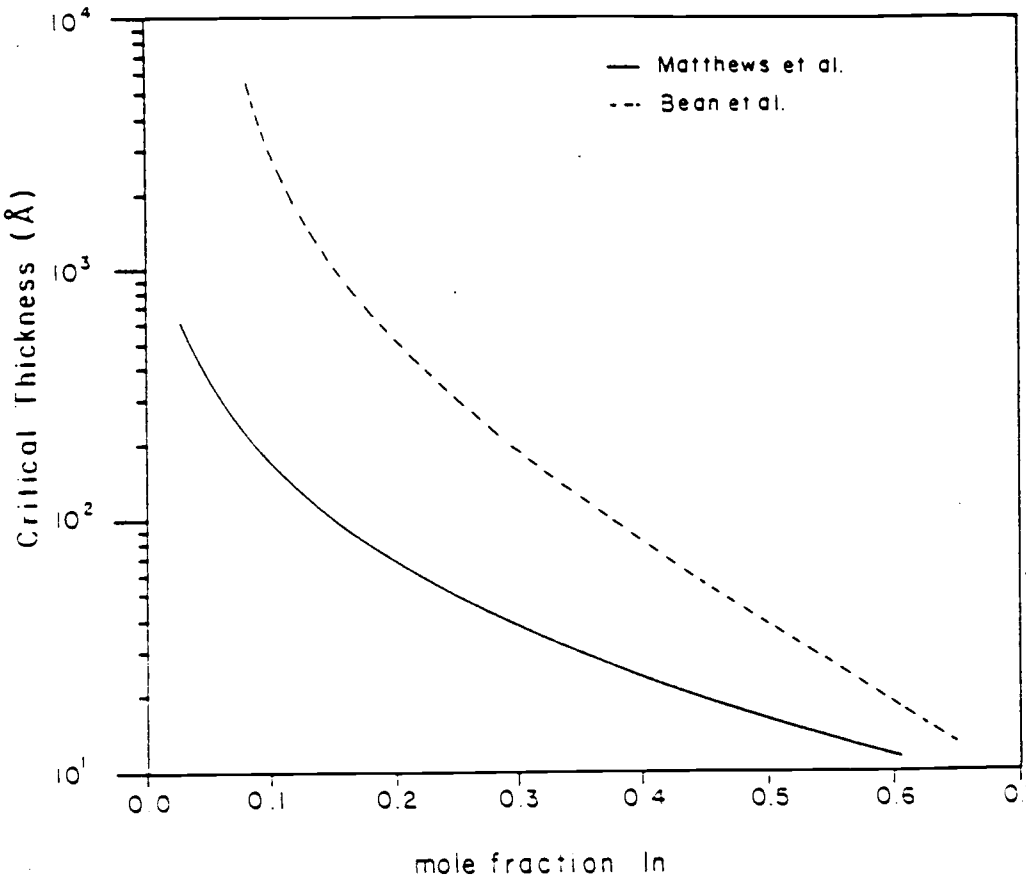

Figure 3.3 Critical thickness for misfit dislocation formation for InGaAs grown on GaAs. The dashed curve was derived from energy density theory and the solid curve from mechanical balance theory[12].

followed by gold. Again, this was achieved by using the Veeco 7760 series metal evaporator. The final sample was packaged, wire bonded and subjected to the transport measurements described below.

Sample (S-2), the layer structure of which is shown on Figure 2.2, was grown using MBE by GAIN Electronics corporation. Photolithographic patterns were first defined onto the sample followed by a wet etch into mesa isolations similar to Figure 3.2 without the bonding pads. Ohmic contacts were then fabricated using electron beam evaporation of Au/Ge/Ni followed by a one minute alloying at 450 °C. The bonding pads were finally deposited using electron beam evaporation of Ti/Pd/Au.

III.2 TRANSPORT MEASUREMENTS

Both Hall and magnetoconductance measurements were made in an Oxford 9/11 Tesla Spectromag-2 superconducting magnet. The data for the Hall measurements were acquired manually and were recorded for temperatures ranging from 1.7 °K to 300 °K at a constant field of 0.32 Tesla. Magnetoconductance measurements, fully computerized, were made at various temperatures below 30 °K.

The block diagram for the experimental set-up is shown in Figure 3.4. For both Hall and magnetoconductance measurements, a constant current of 30 microamps (for sample (S-1)) was maintained between points A and B (Figure 2.5) and the magnetic field applied perpendicular to the surface, in the direction of growth. Temperature dependent Hall voltages were measured between points C and D and the channel voltage was measured between points C and E. The temperature was computer controlled via an

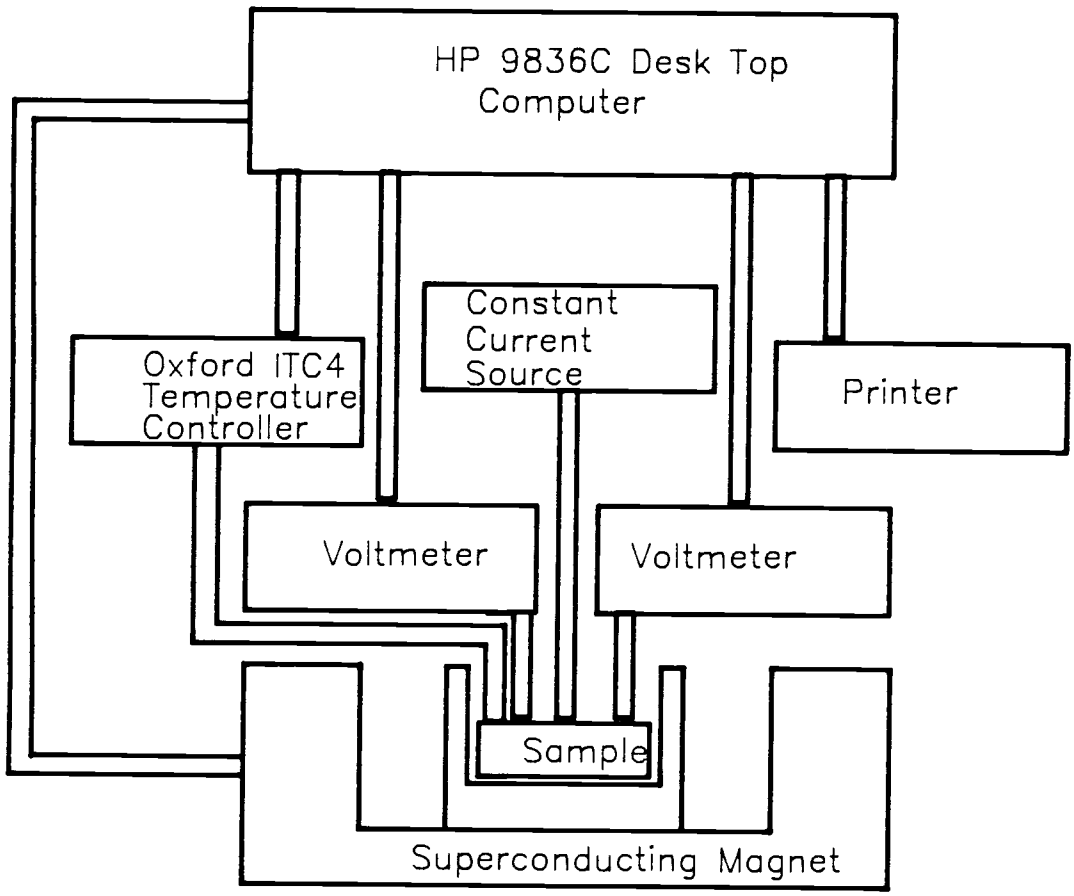

Figure 3.4 Block diagram of Hall and SdH data acquisition system.

Oxford model ITC4 temperature controller and measured by a gold(0.07 atomic iron)-chromel thermocouple. The constant current was provided by a Keithley 220 programmable Current source and the voltages measured by a Tektronix DM 5010 programmable Digital multimeter. From these measurements, it was possible to construct curves of mobility and carrier concentrations versus temperature. The theory and the relevant formulae were discussed in Chapter 2 and the results are presented in Chapter 4.

For Shubnikov de Haas measurements, it was necessary to sweep the magnetic field and monitor the channel voltage concurrently. For this part of the experiment the data acquisition system was completely computerized (Figure 3.4). A Hewlett Packard model 9836C computer was used to gradually sweep and monitor the field between 0 and 8.5 Tesla and at the same time take readings of the channel voltage as measured by a Keithly 181 nanovoltmeter. Here again the constant current was provided by the Keithly 220 programmable current source. The data, consisting of channel voltages and corresponding magnetic fields were stored in ASCII files and later analyzed. The information obtained from these data were carrier concentrations and channel electron effective masses. In order to determine effective masses it was necessary to perform measurements at various temperatures. The effective mass was extracted from the temperature variation of the Shubnikov de Haas oscillations amplitudes as discussed in Chapter 2.

Aside from sample geometry differences, transport measurements on Sample (S-2) were very similar to those of sample (S-1). One notable difference is that for Sample (S-2) a constant current of 1 microampere was used as higher currents resulted in frequent sample blow outs.

IV. EXPERIMENTAL RESULTS

The techniques of low field Hall effect and high field Shubnikov de Haas effect were used to characterize the transport properties of $In_xGa_{1-x}As/Al_yGa_{1-y}As$ heterojunctions on two samples with different values of x, the mole fraction of Indium in the InGaAs material. Hall effect measurements were used to derive both mobility and 2-D carrier concentration versus temperature curves for the temperature range between 1.7 °K and 300 °K. The two samples showed basically the same behavior except that care must be taken in the analysis to take note of the fact that the growth conditions for the two samples were not similar so that their relative mobilities may not have much meaning. These results are presented in section 4.1

Because of thermal damping of the oscillations amplitude, useful SdH data could only be obtained below 30 °K where measurements were made as a function of temperature. The temperature dependent results were used to obtain the carrier effective mass of the channel electrons as described earlier. All the SdH results for the two samples are presented in section 4.2.

The theory of alloy scattering discussed in chapter three showed a relaxation time dependence on the mole fraction of indium in the channel material. The original motivation for studying more than one sample was to investigate the effect of varying the indium mole fraction on the transport properties of InGaAs, especially the mobility dependence. This purpose was to be achieved by studying samples that were grown and processed under the same conditions so that the only variable parameter was the indium mole fraction. This purpose was defeated when it was

discovered that the other samples grown and processed along with Sample (S-1) were of low quality and, therefore, not worth studying. Nevertheless, it was still necessary to have a sample that could, in general, corroborate the results of Sample (S-1). It was with this intention that Sample (S-2) was brought into the study. A look back at chapter three should provide a reminder that the two samples were not just different in their growth and processing techniques but were also quite different in their layer structures. Therefore, the only useful comparisons are in the general behavior of the two samples.

IV.1 HALL MEASUREMENTS RESULTS

IV.1.1 Results for Sample (S-1) (x=0.15)

Table 4-1 shows the measured and calculated Hall effect data for sample (S-1) A slight decrease in the channel voltage is observed between 2 °K and 40 °K followed by a smooth monotonic increase all the way to 300 °K. The Hall voltage on the other hand stays fairly constant upto about 90 °K where it begins to show a slight increase that reaches its highest point around 150 °K. Above 150 °K, the Hall voltage drops continuously with temperature for the rest of the temperature range studied. These results translate into the mobility and carrier concentration curves shown in Figures 4.1 and 4.2, respectively. The dip in the carrier concentration around 150 °K has been observed by other investigators.[53,54] An attempt at explaining the behavior is contained in chapter five, along with the theoretical justification for the observed mobility curves based on the scattering mechanisms in the channel.

Table 4-1 Hall effect data for sample (S-1).

TEMP. (K)	Vhall (mV)	Vchannel (mV)	Mobility cm^2/V-s	Ns (cm-2) *(1E12)
1.7	5.320	24.815	20099	1.128
5.0	5.325	24.775	20150	1.127
17.0	5.325	24.675	20232	1.127
28.0	5.325	24.575	20314	1.127
38.0	5.330	24.540	20362	1.126
48.0	5.330	24.605	20308	1.126
57.5	5.335	24.845	20131	1.125
66.5	5.340	25.280	19803	1.124
75.0	5.340	25.905	19325	1.124
83.5	5.350	26.725	18768	1.121
100.0	5.355	28.965	17332	1.120
109.0	5.355	30.395	16517	1.120
114.0	5.360	31.965	15720	1.119
127.0	5.385	34.055	14824	1.114
137.0	5.415	36.650	13851	1.108
149.0	5.425	39.020	13034	1.106
159.0	5.380	41.185	12247	1.115
169.5	5.325	43.280	11535	1.127
180.0	5.260	45.325	10880	1.141
199.0	5.125	49.250	9756	1.171
220.0	4.935	53.270	8685	1.216
243.0	4.715	57.620	7671	1.273
260.0	4.515	61.395	6894	1.329
284.0	4.320	64.880	6242	1.389
294.0	4.325	66.550	5966	1.417

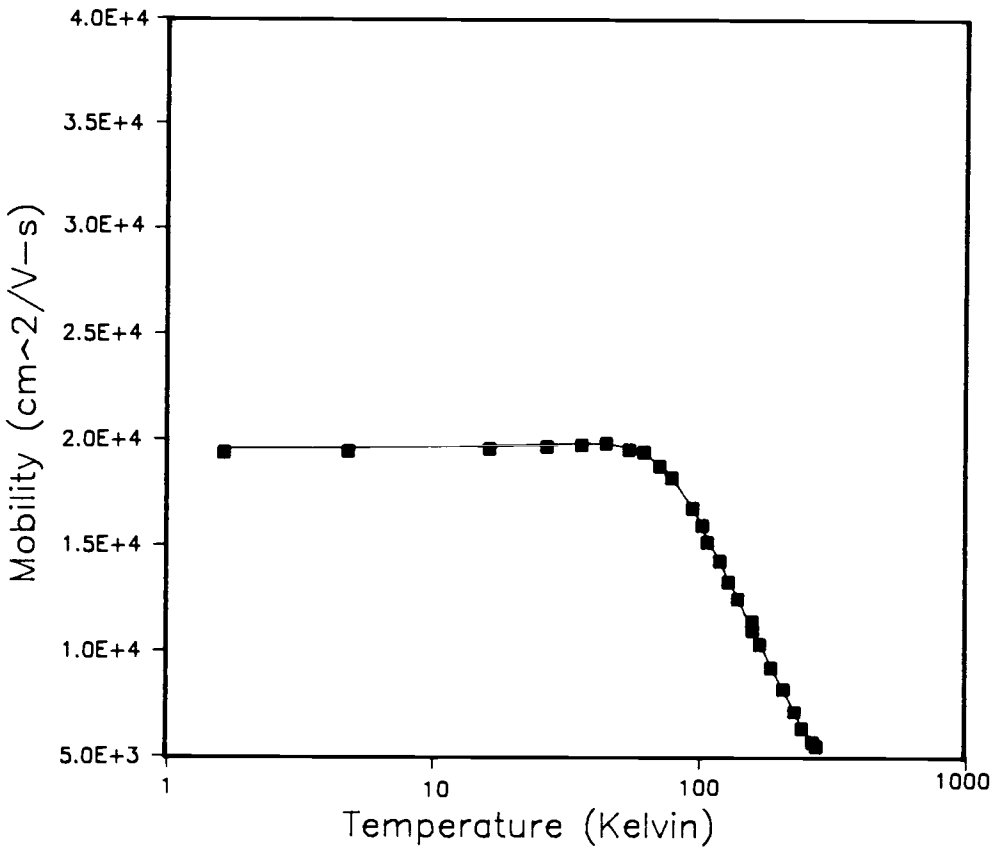

Figure 4.1 Hall mobility versus temperature (semi-log scale) for sample (S-1).

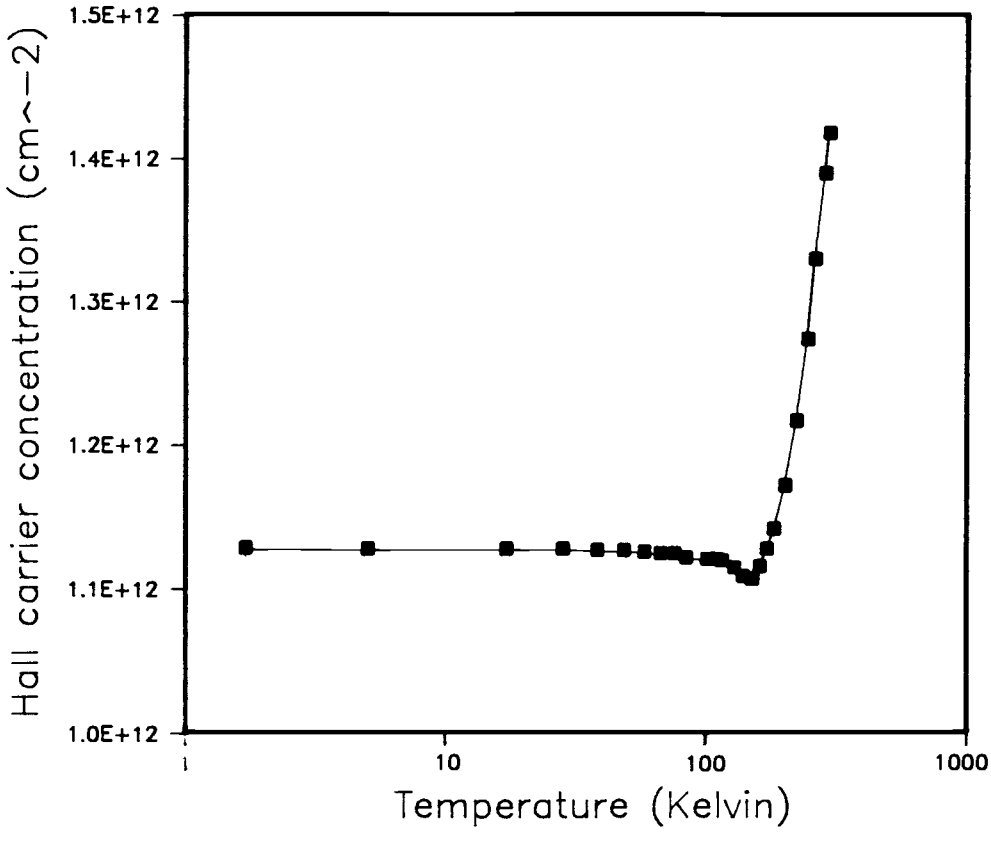

Figure 4.2 Hall carrier concentration versus temperature (semi-log scale) for sample (S-1).

IV.1.2 Results for Sample (S-2) (x=0.25)

The temperature dependent data for this sample are shown in Table 4-2. The results show a similar behavior as the previous sample except that fewer data points were taken resulting in the rather noisier mobility and 2-D carrier concentration curves shown in Figures 4.3 and 4.4, respectively. Both the mobility and carrier concentration are observed to be higher at all temperatures for this sample than sample (S-1). The higher 2-D concentrations are easily explained as the AlGaAS layer in the latter sample was doped to twice the level of the former resulting in a larger electron transfer. A full analysis is deferred till the next chapter.

IV.2 SdH RESULTS

SdH measurements were made at various temperatures and the temperature dependence of the oscillations amplitude used to calculate the effective mass using (2.58). Sample (S-1) was measured at five different temperatures the results of which are shown in Figure 4.5 for three of the temperatures. It can be seen that, as the temperature increases, the oscillation amplitude becomes smaller as expected, with some oscillations disappearing altogether. Similar observations were made for sample (S-2) for which measurements were made at only three temperatures. These results are shown on Figures 4.6 for two of the temperatures. The needed quantities for the determination of the effective mass were obtained from the results and are shown in Tables

4-3 and 4-4 for Sample (S-1) and Sample (S-2), respectively. The effective masses obtained using (2.58) are discussed later in Chapter five.

Table 4-2 Hall effect data for sample (S-2).

TEMP. (K)	Vhall (mV)	Vchannel (mV)	Mobility cm^2/V-s	Ns (cm-2) *(1E12)
1.7	.435	2.8434	25816	1.379
16.0	.435	2.8240	25994	1.379
38.0	.435	2.8225	26008	1.379
47.0	.435	2.8200	26031	1.379
57.0	.435	2.8350	25893	1.379
64.0	.435	2.9400	24968	1.379
73.0	.430	3.0500	23791	1.395
83.0	.435	3.1900	23011	1.379
109.5	.435	3.6900	19893	1.379
127.5	.435	4.1250	17795	1.379
148.0	.4375	4.7200	15642	1.371
178.0	.4400	5.6850	13061	1.364
204.5	.435	6.5800	11160	1.379
227.0	.434	7.3800	9924	1.382
260.0	.4275	8.4335	8554	1.404
290.7	.418	9.4000	7504	1.435

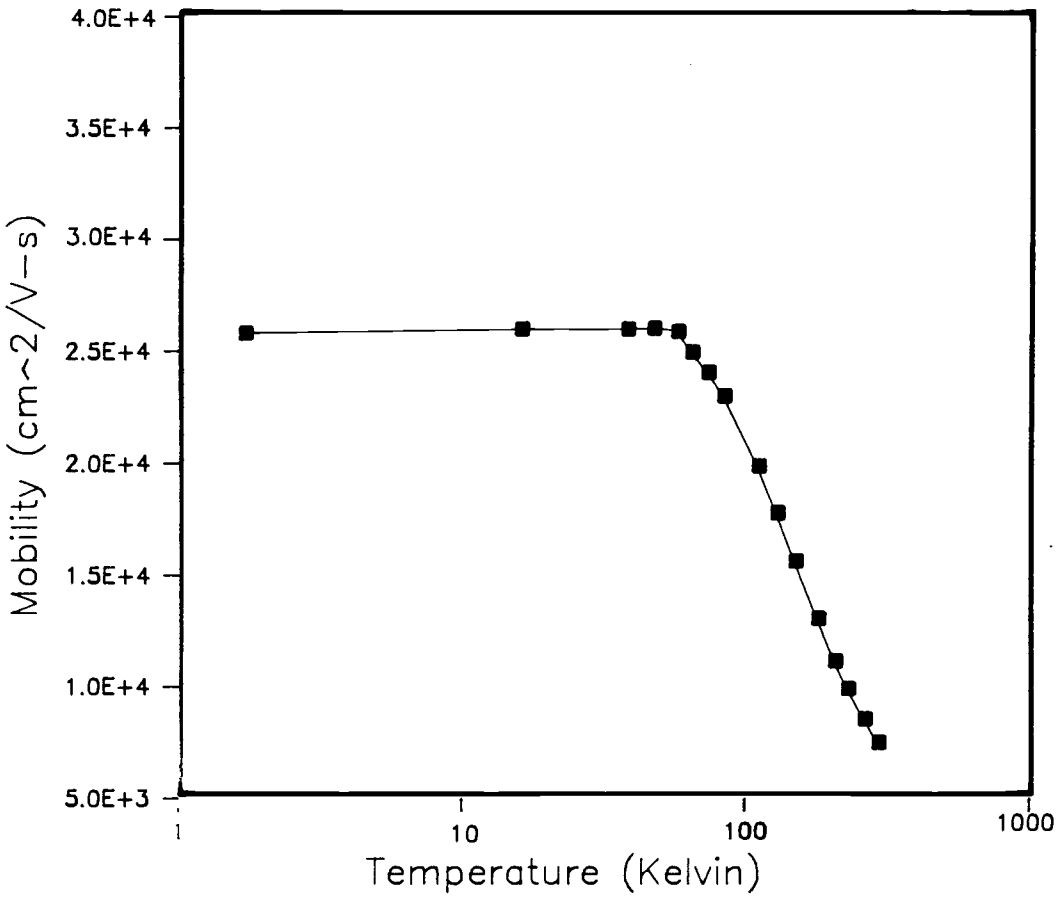

Figure 4.3 Hall mobility versus temperature (log-log scale) for sample (S-2).

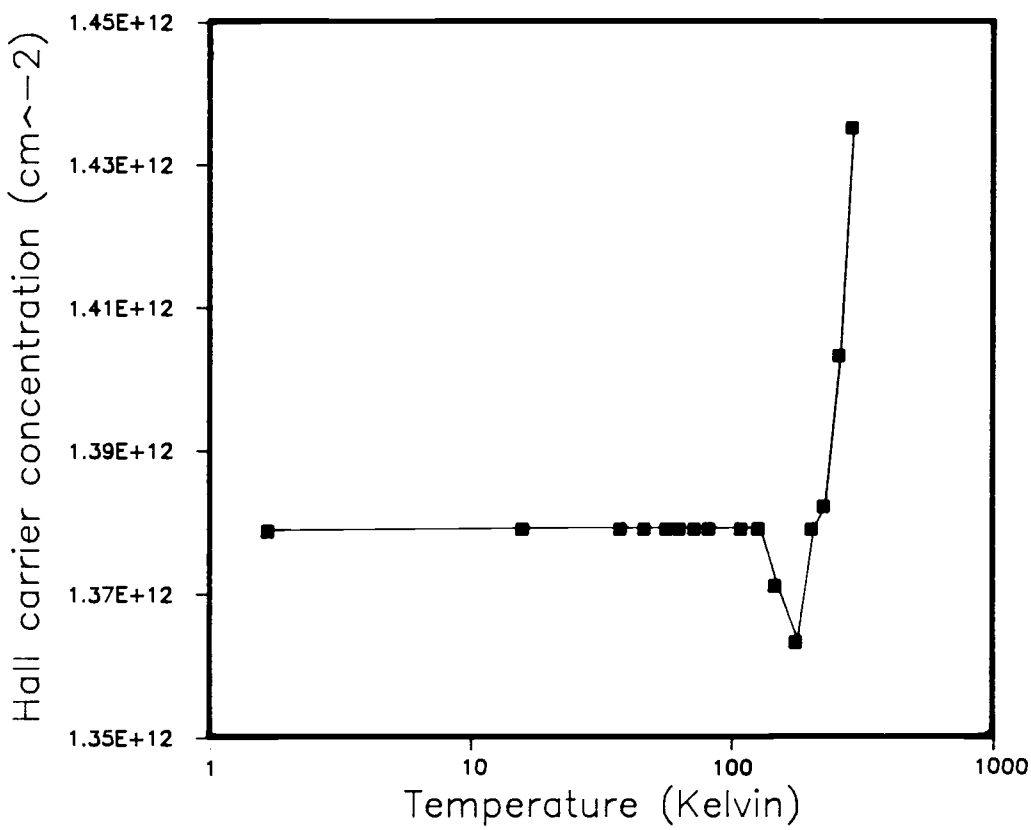

Figure 4.4 Hall carrier concentration versus temperature (semi-log scale) for sample (S-2).

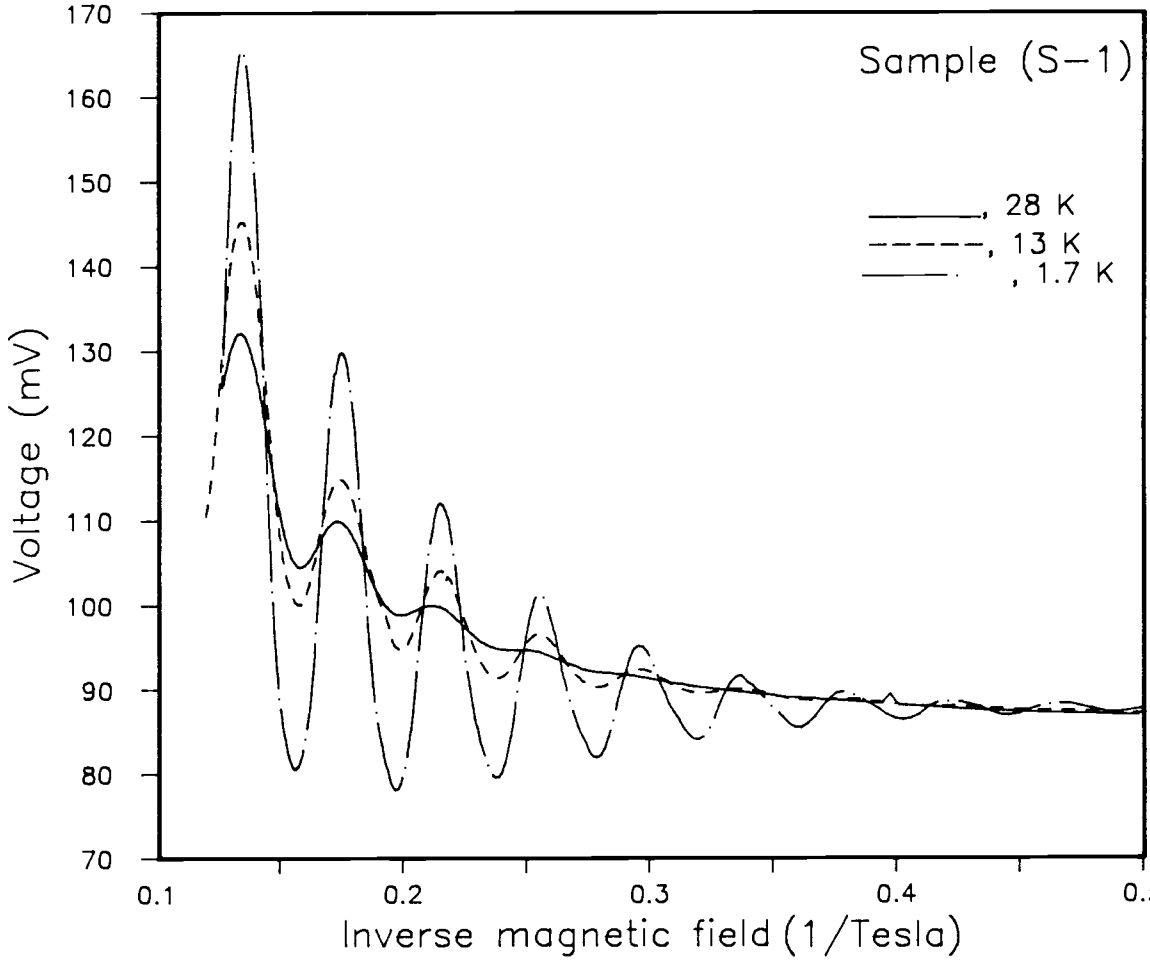

Figure 4.5 SdH oscillations for sample (S-1) at 1.7 °K, 13 °K, and 28 °K.

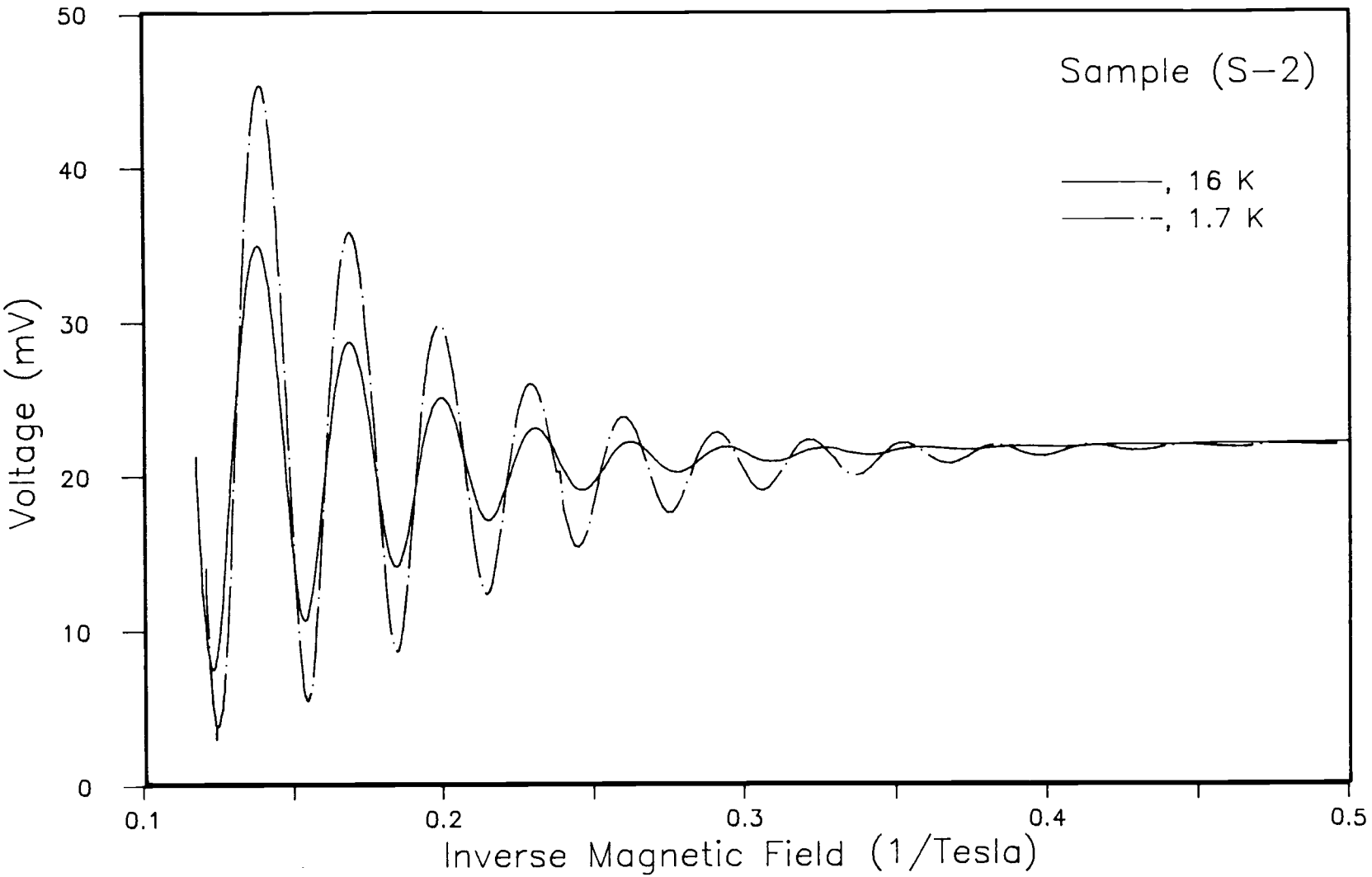

Figure 4.6 SdH oscillations for sample (S-2) at 1.7°K.and 16 °K.

Table 4-3 Data for determining the effective mass of InGaAs electrons for sample (S-1).

Mag. fld. (Tesla)	Ampltd. (1.7K)	Ampltd. (6K)	Ampltd. (13K)	Ampltd. (20K)	Ampltd. (28K)
7.55	1	0.833	0.530	0.392	0.326
5.67	1	0.838	0.386	0.265	0.215
4.63	1	0.814	0.388	0.194	0.160
3.85	1	0.818	0.325		

Table 4-4 Data for determining the effective mass of InGaAs electrons for sample (S-2).

Mag. fld. (Tesla)	Ampltd. (1.7K)	Ampltd. (7K)	Ampltd. (16K)
7.27	1	0.874	0.599
5.95	1	0.834	0.529
5.03	1	0.820	0.450
4.35	1	0.783	0.379
3.83	1	0.753	0.315
3.41	1	0.713	0.252

V. ANALYSIS OF RESULTS

A theory for the behavior of a two dimensional electron gas in III-V compounds was developed in chapter 2. In chapter 4, experimental results were presented for transport measurements at InGaAs/AlGaAs heterojunctions and it is hoped that the behavior observed should be explicable within the limits of the theory. The purpose of the present chapter is to apply the theory of chapter 2 to try to meaningfully explain the observed results.

V.1 HALL CARRIER CONCENTRATION VERSUS TEMPERATURE RESULTS

Results for the temperature dependent Hall carrier concentration were shown on Tables 4-1 and 4-2 for samples (S-1) and (S-2), respectively. The corresponding curves appeared as Figures 4.2 and 4.4. A dip in the carrier concentration is evident at around 150 °K for sample (S-1) and at a somewhat higher temperature for sample (S-2). This behavior is likely to be caused by the presence of parallel conduction in the AlGaAs layer and may be understood as follows: The Hall technique measures not only the two-dimensional carrier concentration but the total carrier concentration of all the charges participating in the conduction process. For aluminum mole fractions greater than 20%, the occurrence of DX centers becomes effective. These are deep level traps with energies on the order of 0.25 eV. At room temperature, in the presence of ambient room light, some of the carriers in the trap will have enough energy to overcome the barrier and get excited to the conduction band. In addition

there will also be present in the AlGaAs layer charges that did not get transferred to the InGaAs layer. This is the condition of the sample just before inserting it into the liquid Helium cryostat. As soon as the sample is dipped into the cryostat, these carriers are frozen in the conduction band and cannot get back into the trap since they do not have enough energy to overcome the small barrier between their state in the conduction band and the trap. The Hall carrier concentration between 2 °K and around 100 °K is fairly constant and represents the combined count of these carriers in the AlGaAs layer conduction band and the two-dimensional carriers in the InGaAs channel. As temperature is increased further, the carriers in the AlGaAs layer acquire enough thermal energy to overcome the small barrier and get back into the trap. At around 150 °K, the center of the dip, all the AlGaAs carriers have supposedly been deactivated into the trap. A further increase in temperature gives the entrapped carriers enough energy to overcome the deep level barrier and become available for conduction once more. Higher temperatures, in addition to activating more deep level carriers, results in thermal ionizations, the combined effect of which creates the monotonic increase in carrier concentration with temperature observed above 150 °K. The foregoing explanation is very qualitative and may not readily provide a clear understanding of the situation that exists. In fact, the above explanation should only be good for measurements taken from the lower to the upper temperature limit and not vice versa. A more quantitative approach is, obviously needed, but is beyond the scope of present considerations.

V.2 HALL MOBILITY VERSUS TEMPERATURE RESULTS

A theory based on the scattering mechanisms in the two-dimensional channel was worked out to explain the experimental mobility versus temperature results. In formulating the theory, it was assumed that only the lowest subband was occupied and that the wave functions were confined within the channel. Possible effects of these assumptions are discussed shortly.

In the limits of the above mentioned assumptions the calculation of the scattering rates for the various scattering mechanisms was carried out in the framework of the Boltzmann transport equation. Within this framework the scattering rate is expressed as

$$\Gamma_{kk'} = \frac{2\pi}{\hbar} |V_{kk'}|^2 \delta(E_{k'} - E_k + \hbar w) \tag{5.1}$$

where $V_{kk'} = \langle k'|V(r)|k\rangle$ is the matrix element for the scattering potential, $V(r)$, in the unperturbed states, k and k'. In two dimensions the relaxation time for the i^{th} scattering mechanism is

$$\frac{1}{\tau_i(E)} = \frac{A}{4\pi^2} \int dk'(1-\cos\theta_k)\, \Gamma_{kk'} \tag{5.2}$$

The mobility is calculated from this as

$$\mu = \frac{e\langle\tau_i\rangle}{m^*} \tag{5.3}$$

Here $\langle\tau_i\rangle$ is the average momentum relaxation time and is found from the Boltzmann equation as

$$\langle \tau_i \rangle = \frac{\int_0^\infty dE\ E\ \tau_i(E) \frac{\partial f}{\partial E}}{\int_0^\infty dE\ E\ \frac{\partial f}{\partial E}} \qquad (5.4)$$

where f is the Fermi-Dirac distribution function. The total relaxation time for all the scattering mechanisms is obtained using Mathiessen's rule as

$$\left\langle \frac{1}{\tau} \right\rangle = \sum_i \left\langle \frac{1}{\tau_i} \right\rangle \qquad (5.5)$$

It should be noted that relaxation time aproximation is only valid for elastic scattering processes or isotropic inelastic scattering mechanisms.. This is not the case with polar optical phonon scattering, although such an assumption was made. The same assumption was made by Tsui et al.[57] Theoretical mobilities obtained in the manner described above based on the scattering mechanisms discussed in Chapter 2 are shown in Figures 5.1 and 5.2 for samples (S-1) and (S-2), respectively.

The experimental mobilities obtained for the two samples were not too different, with sample (S-2) consistently showing higher values for all temperatures considered. For both samples a small initial increase in mobility with temperature is observed between 1.7 °K and approximately 40 °K where it peaks off and then starts a gradual decrease that becomes almost linear in a log-log scale above 100 °K. These curves follow the general behavior for two-dimensional structures. The initial rise in mobility has been observed by other authors[57] and has been explained to be typical of low mobility samples in cases where remote impurity scattering is the dominant mechanism at low temperatures. Here the slight increase can be attributed to the importance of remote impurity, background impurity, and alloy scattering at these temperatures.

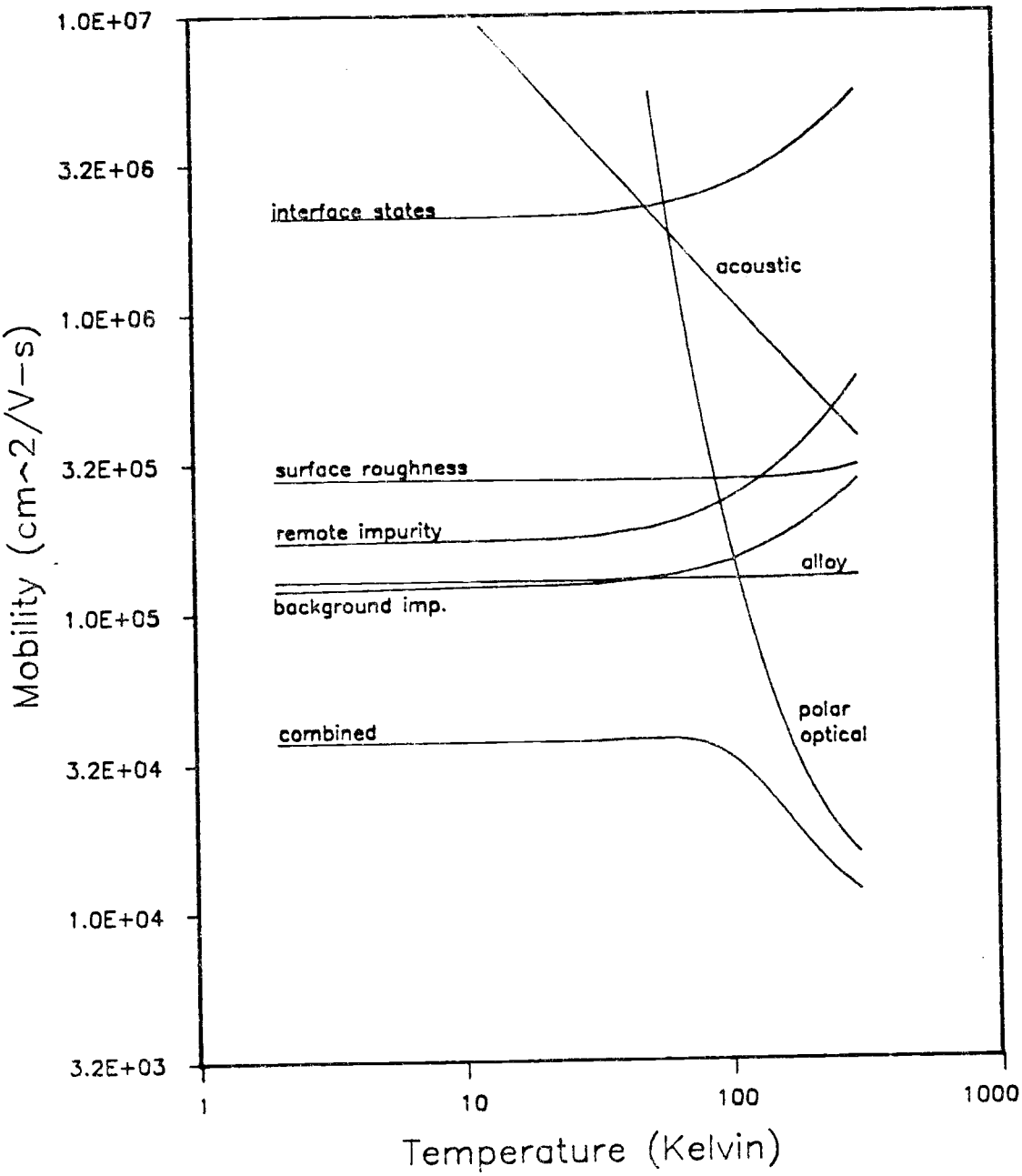

Figure 5.1 Theoretical mobility limited by the various scattering mechanisms (log-log scale) for sample (S-1). See Appendix A for the parameters used.

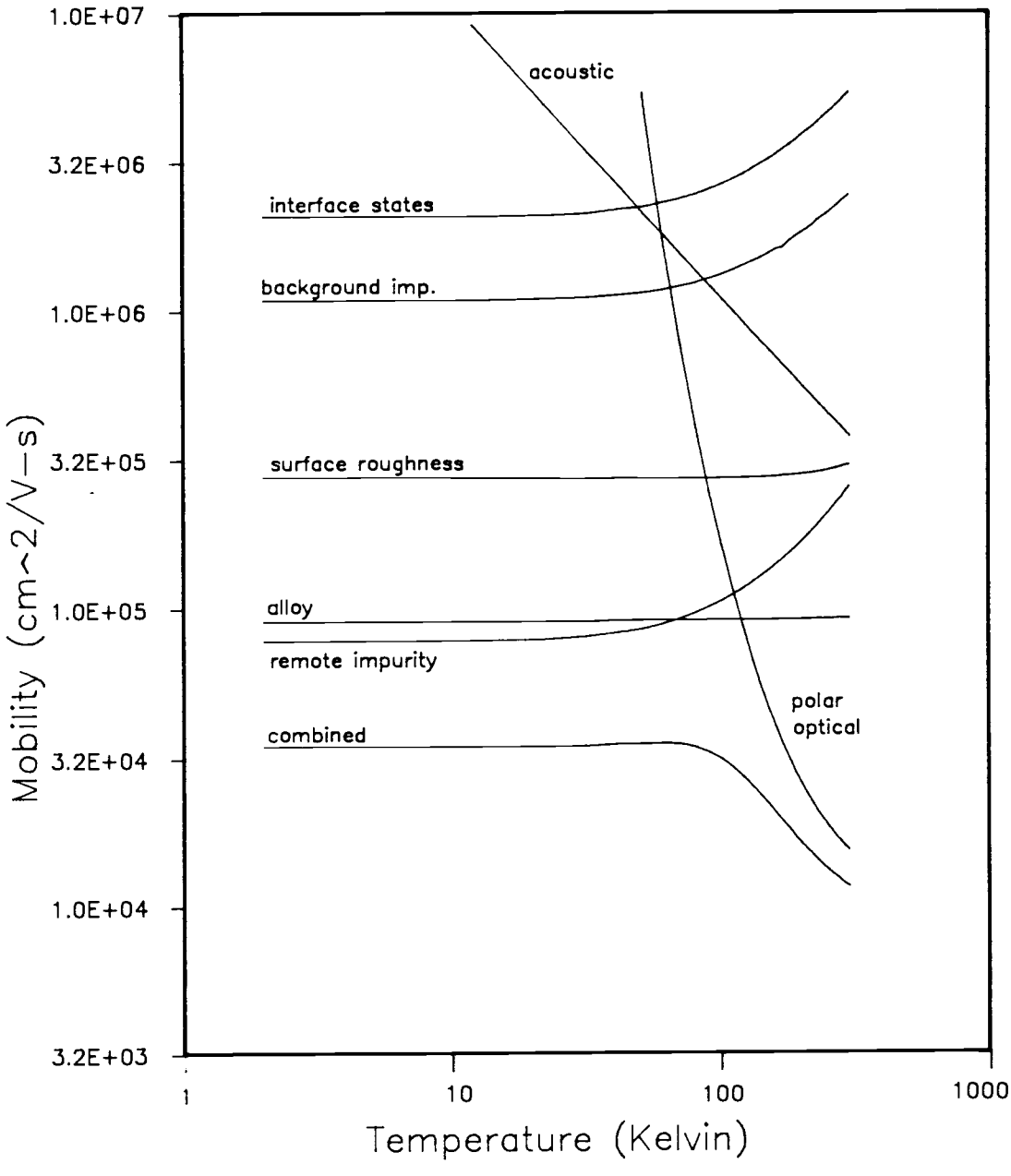

Figure 5.2 Theoretical mobility limited by the various scattering mechanisms (log-log scale) for sample (S-2). See Appendix B for parameters used.

Theoretical calculations show that the mobility limited by alloy scattering is temperature independent and is around 1.5×10^5 $cm^2/V\text{-}s$ for sample (S-1) (see Figure 5.1). Remote impurity and background impurity scattering limited mobilities, on the other hand, constantly increase with temperature in an almost exponential manner. For temperatures below 40 °K, the region where the initial increase is observed, the mobilities limited by the three mechanisms are very close and the slight increase can be attributed to the influence of the increasing remote and background impurity scattering limited mobilities.

It is surprising that the higher mole fraction sample (S-2) shows a higher mobility than the low mole fraction sample (S-1). Provided that no dislocations resulted during sample growth and, given that the purity of the samples are the same and that the structures are similar, the mobility for the two samples should only differ by factors introduced by differences in effective mass and alloy scattering which, as was seen in chapter 2, has a relaxation time that depends on the mole fraction of Indium in the compound. Theoretical results shown on Figures 5.1 and 5.2 indicate that the higher the indium mole fraction, the more limited should be the mobility due to alloy scattering and, since alloy scattering is the dominant mechanism at low temperatures, the overall mobility is also lower for the lower mole fraction sample. This contradicts the observed experimental results. As mentioned earlier, a rigorous comparison of the results for the two samples is impossible owing to the fact that the growth conditions and preparation techniques were not identical. Possible explanations for the discrepancy are that sample (S-1) may possess a greater number of background impurities and interface states than sample (S-2). An increase in both of these

quantities lowers the relevant individual mobilities and should result in a lower overall mobility as well. The general behavior of the mobility versus temperature curve is, however, very similar for the two samples.

It can be seen from Figures 5.1 and 5.2 that alloy scattering is the mobility limiting factor at low temperatures closely seconded by remote impurity scattering while optical phonon scattering dominates at high temperatures. Background impurity scattering appears to be very limiting at low temperatures for sample (S-1) but the background impurity concentration was not known with certainty and was treated as an adjustable parameter. For very pure samples, this scattering mechanism can be very negligible. The mobilitiy limited by all the scattering mechanisms combined, together with the experimental curve are shown in Figure 5.3 for sample (S-1) and in Figure 5.4 for sample (S-2). Aside from being slightly higher, the theoretical curves show general qualitative agreement with experiment.

The disagreement may be explained by the influence of several factors: The assumption that the wavefunction of the electron is confined to the channel ignores possible contributions to alloy scattering from the AlGaAs layer. Inclusion of this would reduce the mobility limited by alloy scattering. Since alloy scattering is the dominant mechanism at low temperatures, this would lower the flat part of the theoretical mobility curve improving agreement with experiment. Possible occupation of higher subbands, however, should only have effect at higher temperatures and may improve the fit up there.

It should also be noted that the relaxation times for the various scattering mechanisms have some adjustable parameters which can be varied to improve the fit. The quantity $\langle V_o \rangle$ appearing in the relaxation time

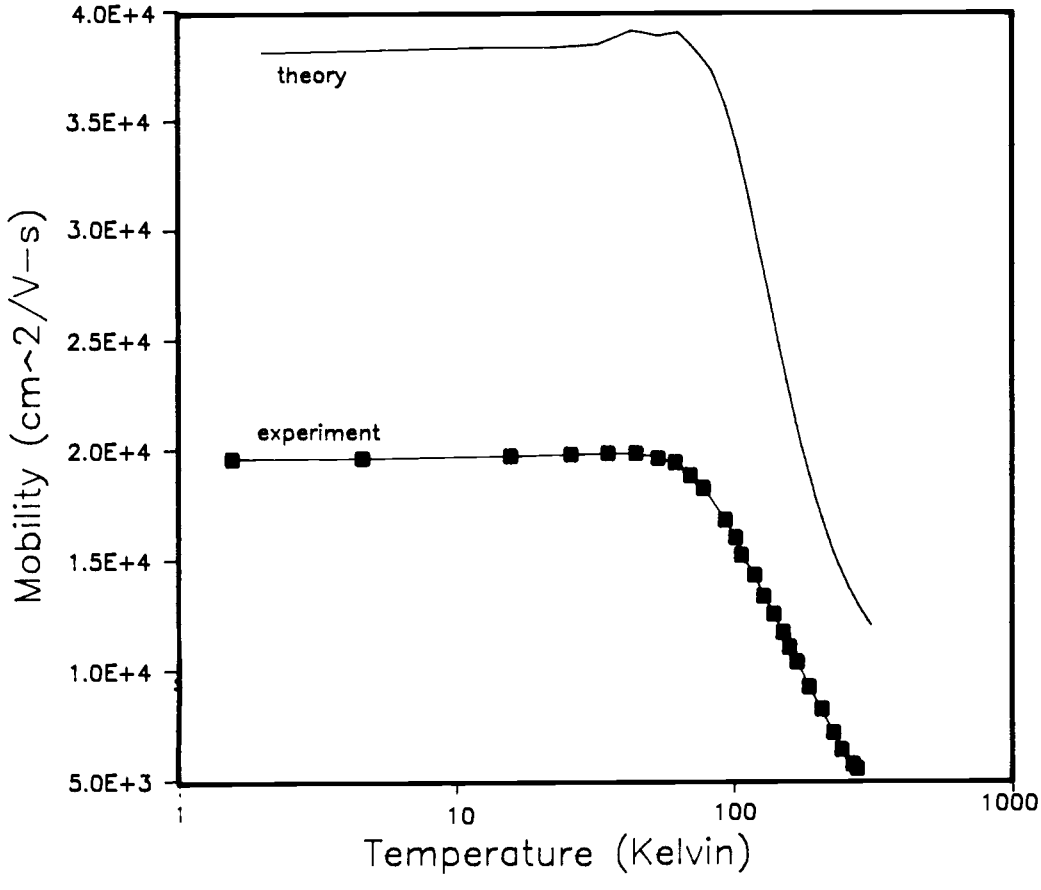

Figure 5.3 Hall mobility versus temperature (semi-log scale) for sample (S-1). The alloy scattering potential and the background impurity concentration used to derive the theoretical curve were 0.6 eV and $4.35 \times 10^{16}/cm^3$, respectively. Notice the bad fit between theory and experiment compared to Figure 5.5 where these parameters have been adjusted.

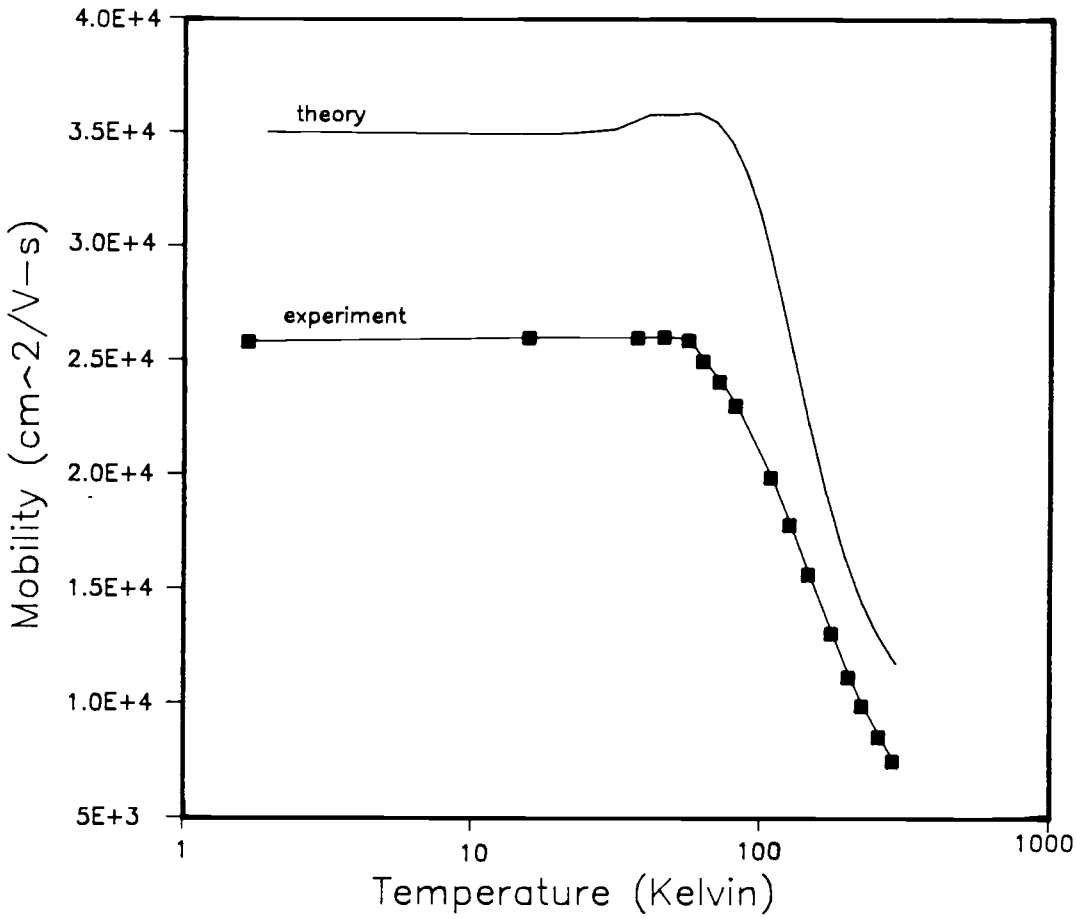

Figure 5.4 Hall mobility versus temperature (semi-log scale) for sample (S-2). The alloy scattering potential and the background impurity concentration used to derive the theoretical curve were 0.6 eV and $5\times10^{15}/cm^3$, respectively. Notice the bad fit between theory and experiment compared to Figure 5.6 where these parameters have been adjusted.

for alloy scattering (Equation 2.44) is obtained by fitting the low temperature bulk mobility data. The value most used in the literature is 0.6 eV[55], the bulk InGaAs value. Higher values shifts the mobility plateau down and thus improves agreement with experiment. The possibility of higher scattering potentials for the samples of the present study may be justified by the possible effects of strain, which is not present in the bulk. Other adjustable parameters are density of surface states associated with interface scattering, background impurity concentration, remote impurity concentration, correlation length and the rms height for surface roughness. Adjusting interface states and surface roughness parameters are not expected to make much difference as these mechanisms are not important at all temperatures as shown in Figures 5.1 and 5.2. Increasing background and remote impurity concentrations should all result in a lower overall mobility. These quantities are treated as fit parameters because they are not known with certainty. The theoretical curves appearing in Figures 5.3 and 5.4 were calculated using the standard bulk value of the fluctuating alloy potential, 0.6 eV, and the expected background impurity concentration of 4.35×10^{16} cm^{-3} and 5*1015 cm-3 for samples (S-1) and (S-2), respectively. The fit between theory and experiment is seen to be poor. In Figures 5.5 and 5.6 the fits have been improved by adjusting both the alloy scattering potential and the background impurity concentration. The high temperature fit, however, continues to be minimal and this may be due to the possible discrepancies between the actual and the assumed polar optical phonon model and the omission of intersubband scattering.

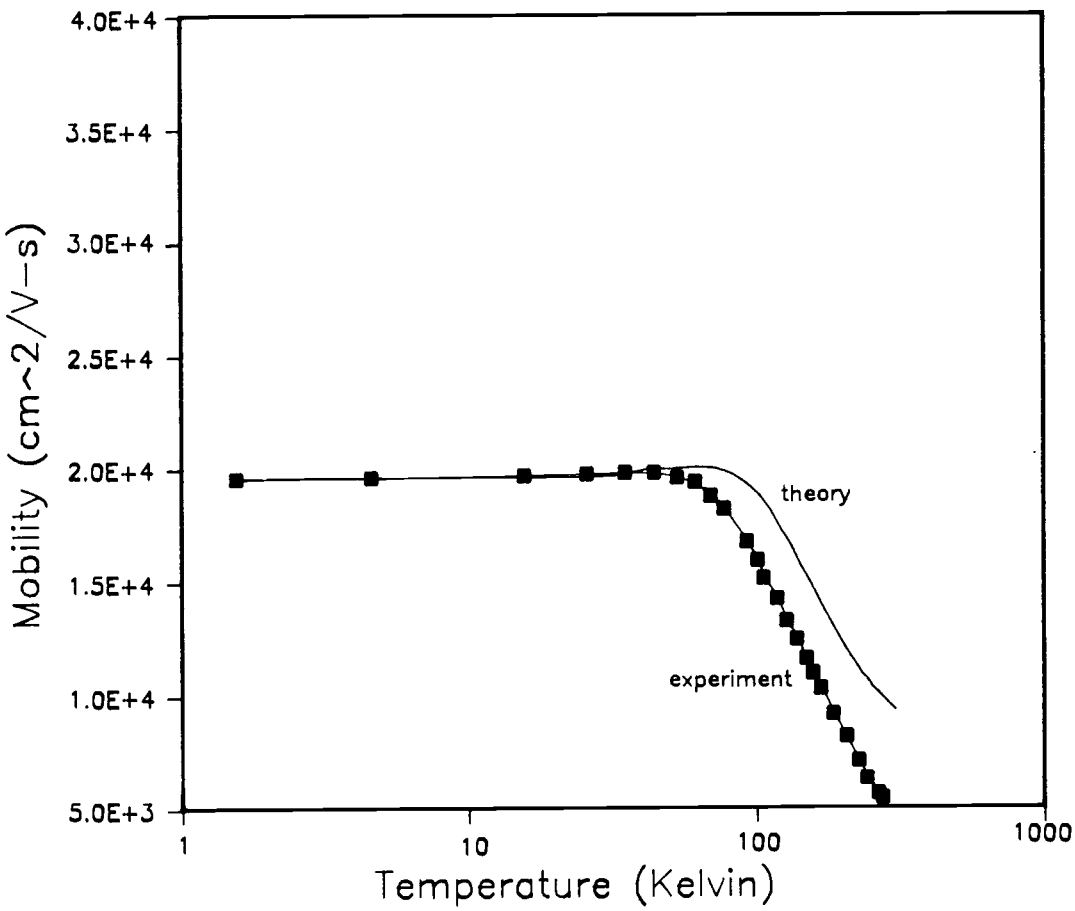

Figure 5.5 Hall mobility versus temperature (semi-log scale) for sample (S-1). The alloy scattering potential and background impurity concentration have been adjusted 1 eV and $9\times10^{16}/cm^3$, respectively. Notice the improved fit between theory and experiment compared to Figure 5.3. See text for details.

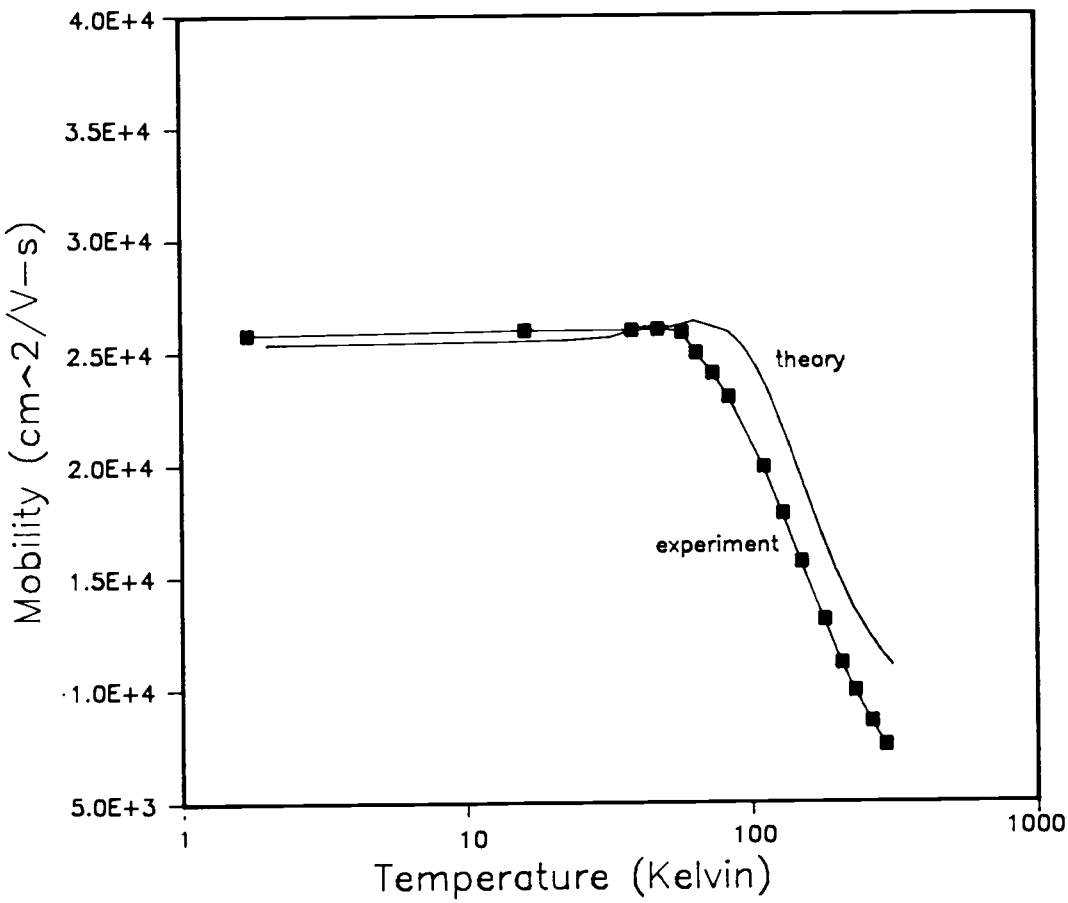

Figure 5.6 Hall mobility versus temperature (semi-log scale)for sample (S-2). The alloy scattering potential and background impurity concentration have been adjusted to 0.66 eV and $4.35 \times 10^{16}/cm^3$, respectively. Notice the improved fit between theory and experiment compared to Figure 5.4. See text for details.

V.3 EFFECTIVE MASS RESULTS

To determine the effective mass from the SdH oscillations, (2.58) was fitted to experimental amplitude versus temperature data using non-linear least squares techniques. The form of (2.58) suggests that in the limit as temperature approaches zero, the amplitude should approach unity. Accordingly, the data points used in the analysis were normalized so that the amplitude was equal to unity when the temperature was lowest. Figure 5.7 shows what the fit looks like for sample (S-1) at one of the four field points investigated. Plots such as these are called massplots.[42] Similar representative plots for sample (S-2) are shown in Figure 5.8.

It is apparent from Tables 5-1 and 5-2 that the effective mass for the two samples exhibits a positive coefficient magnetic field dependence. Behavior such as this has been observed by a number of investigators in both bulk and two dimensional structures but the variations they observed were miniscule compared to present observations.[42,43,58]

The expected $In_xGa_{1-x}As$ electrons effective mass for the two samples studied can be obtained by a linear extrapolation of the results for GaAs (x=0) and for InAs (x=1). The values for the binary materials are $0.067m_e$ and $0.023m_e$, respectively. The relevant expression for the extrapolation is then

$$m^* = 0.067m_e - 0.044x \qquad (5.6)$$

Using (5.19), the predicted results are $0.0604m_e$ for sample (S-1) and $0.056m_e$ for sample (S-2).

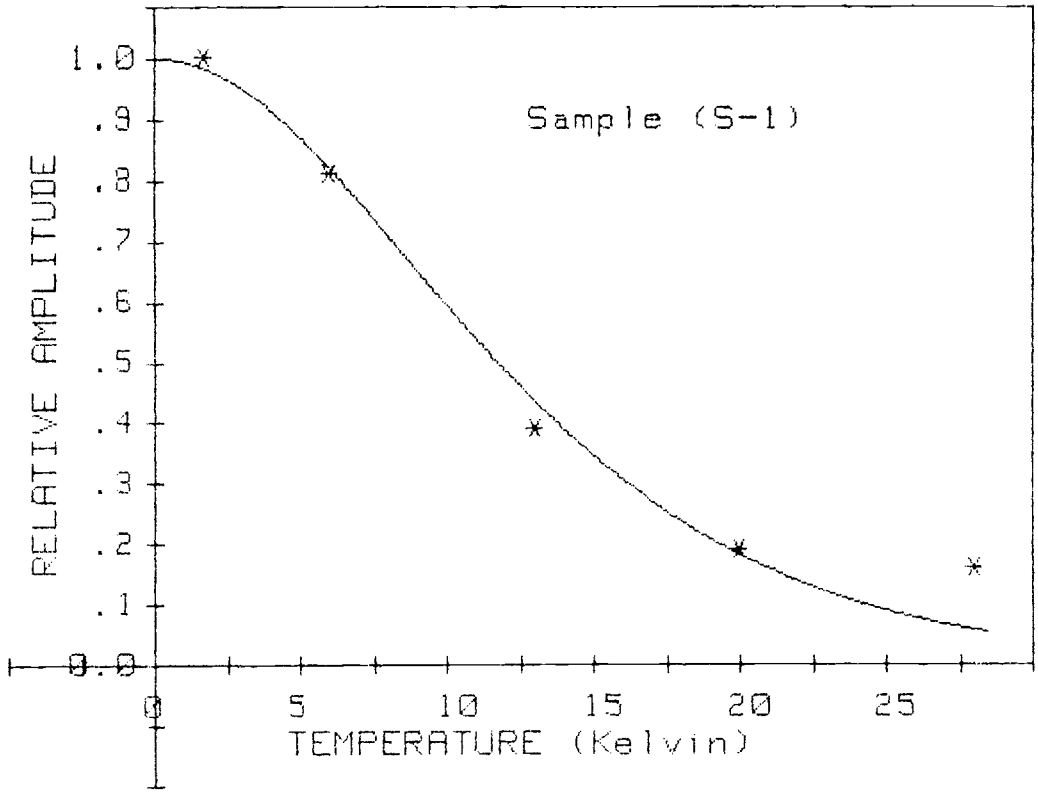

Figure 5.7 Massplot for sample (S-1) at 4.63 Tesla.

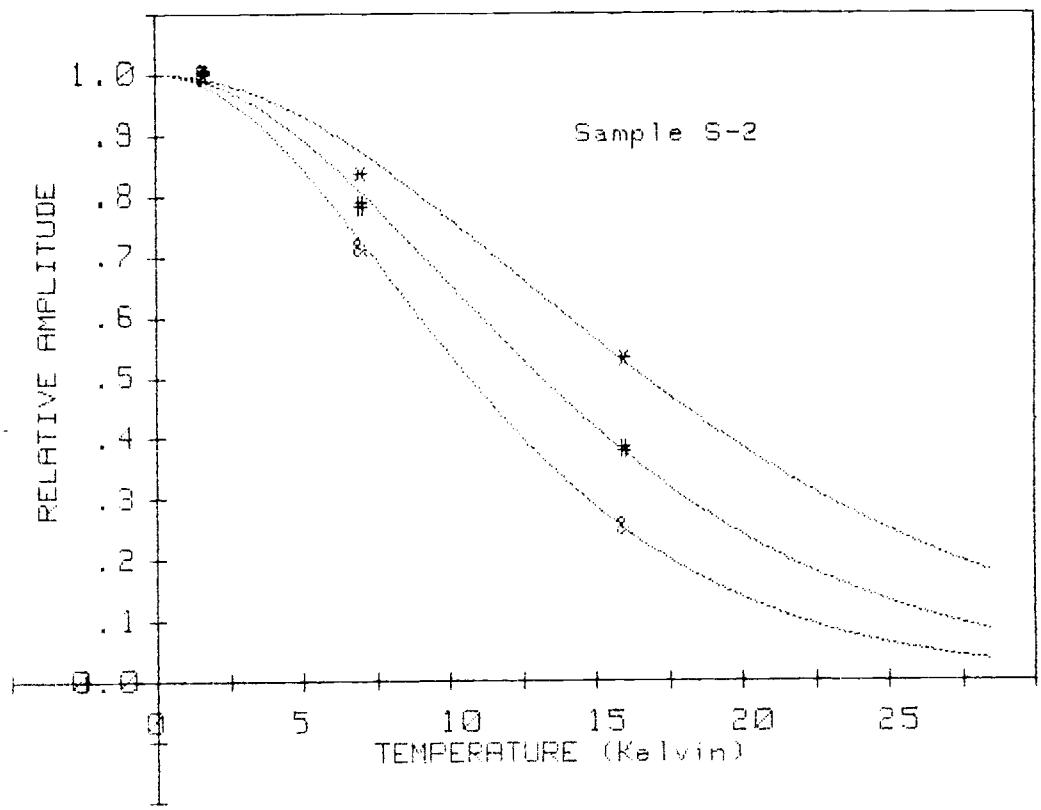

Figure 5.8 Massplots for sample (S-2) at 3.41, 4.35, and 5.95 Tesla in that order from the bottom curve.

Table 5-1 Data showing the dependence of effective mass on magnetic field for sample (S-1).

Mag. fld. (Tesla)	Effctv. mass
7.55	0.067
5.67	0.066
4.63	0.059
3.85	0.055

Table 5-2 Data showing the dependence of effective mass on magnetic field for sample (S-2).

Mag. fld. (Tesla)	Effctv. mass
7.27	0.057
5.95	0.053
5.03	0.051
4.35	0.049
3.83	0.048
3.41	0.047

For sample (S-1), the highest of the four field points at which the mass was measured was 7.55 Tesla while the lowest was 3.85 Tesla. The masses obtained were $0.067m_e$ and $0.055m_e$ for the two fields, respectively. Thus, for a field variation of 3.70 Tesla, the mass varied by $0.12m_e$ which is a 19.6% difference. Mass measurements for sample (S-2) were done at six field points. Here the lowest and highest fields were 7.27 and 3.41 Tesla for which the masses obtained were $0.057m_e$ and $0.047m_e$, respectively. A variation of 3.86 Tesla in field thus resulted in a mass variation of $0.01m_e$ for this sample. This represents a mass difference of 19.2%. Two observations can be made from these results: Firstly, although the experimental results are variable with field, the results for sample (S-1) are generally higher than those for sample (S-2), in agreement with theory; secondly, the mass variation with field for the two samples show fairly similar behavior indicating that the effect may not just be a random occurrence.

One possible source of mass enhancement in an applied magnetic field has been given by Das Sarma[59,60] in which he addressed, from a theoretical standpoint, the polaronic mass renormalization in weakly polar two-dimensional structures. In polar materials like InGaAs, the two dimensional electrons weakly couple to the longitudinal optical (LO) phonon of the bulk resulting in a modification of the electron effective band mass from m^* to $m^{**} = m^*(1 + \pi\alpha/8)$.[59] In this expression α is the Frohlich coupling constant and is of order 0.1[60] for weakly polar materials like InGaAs. The above result for the renormalized mass is based on the assumption that there is no screening and that the wave functions are purely two-dimensional. Indeed these assumptions are purely for mathematical convenience and do not exactly reflect the

situation that exists. The effect of these factors, when included, is to reduce the effective interaction between the confined electrons and the LO-phonons resulting in a less[59] enhanced mass than the one obtained by excluding them.

An understanding of the effect on the effective mass of applying a magnetic field normal to the 2-D electron gas is best achieved by starting from the expression for the electronic energy. In the presence of an external magnetic field B, the energy of a bare 2-D electron, neglecting non-parabolicity, is given by

$$E_n = (n + 1/2)\ \hbar w_c \tag{5.7}$$

where $w_c = eB/m^*$ is the cyclotron frequency with m^* and n the bare band effective mass and the relevant Landau level index, respectively. In the presence of electron-LO phonon coupling, the electronic energy shift δE_n is given by[60]

$$\delta E_n = \sum_{n'} \sum_{q} \left[\frac{|u_{nn'}(q)|^2}{\hbar}\right] \left[(n-n')w_c - w_{LO}\right]^{-1} \tag{5.8}$$

Here w_{LO} is the LO-phonon frequency and $u_{nn'}(q)$ is the coupling term given by

$$|u_{nn'}(q)|^2 = \left(\frac{2\pi\alpha}{q}\right)\left(\frac{\hbar}{2m^* w_{LO}}\right)^{1/2} \hbar^2 w_{LO}^2 V_{nn'}(q) \tag{5.9}$$

with

$$V_{nn'}(q) = \left(\frac{n_2}{n_1}\right)\left(\frac{q^2\rceil^2}{2}\right)^{n_1-n_2} e^{-q^2\rceil^2/2} \left[L_{n_2}^{(n_1-n_2)}\left(\frac{q^2\rceil^2}{2}\right)\right]^2 \tag{5.10}$$

where $l = (ch/eB)^{1/2}$ is the Landau length, $n1 = \max(n,n')$, $n2 = \min(n,n')$, and L is the associated Laguerre polynomial.

In his analysis, Das Sarma considered explicitly three different regimes of which only one will be of interest here: weak magnetic field ($w_c << w_{LO}$); strong magnetic field ($w_c >> w_{LO}$), resonant magnetic field ($w_c \approx w_{LO}$). Only the first regime is considered here as the others do not fit the conditions of the present work. This can be understood as follows: For InGaAs, the phonon energy $\hbar w_{LO} \approx 35$ meV which implies that $w_{LO} = 5.30\times10^{13}$ s^{-1}. The highest magnetic field used in the present work was 7.55 Tesla which corresponds to $w_c = 2.21\times10^{13}$ s^{-1}, assuming $m^* = 0.06m_e$, the expected effective mass for 15% Indium InGaAs electrons. This value of w_c is seen to be less that w_{LO} implying that all the field points investigated satisfied the first regime, ($w_c << w_{LO}$). If it is assumed that only the ground state is occupied the zero order (n=0) energy shift is given by[60]

$$\delta E_0 = -\sum_{n'q} \sum \left[\left| u_{0n'}(q) \right|^2 (n' w_c + w_{LO}) \hbar \right] \tag{5.11}$$

Using w_c/w_{LO} as a small expansion parameter and including only terms upto w_c^2/w_{LO}^2, the ground state energy shift expression becomes

$$\delta E_0 = -\hbar w_{LO} \left[\frac{\pi\alpha}{2} + \frac{\pi\alpha}{16} \left(\frac{w_c}{w_{LO}}\right) + \frac{9\pi\alpha}{512} \left(\frac{w_c}{w_{LO}}\right)^2 \right] \tag{5.12}$$

whereas the first excited Landau level shift is

$$\delta E_1 = -\hbar w_{LO} \left[\frac{\pi\alpha}{2} + \frac{3\pi\alpha}{16} \left(\frac{w_c}{w_{LO}}\right) + \frac{81\pi\alpha}{512} \left(\frac{w_c}{w_{LO}}\right)^2 \right] \tag{5.13}$$

For the 0 to 1 transition,[60]

$$w_c^* = \frac{(E_1^* - E_0^*)}{\hbar} \tag{5.14}$$

where $E_1^* = E_1+\delta E_1$ and $E_0^* = E_0+\delta E_0$. After substitution, the final expression is

$$w_c^* = w_c\left[1 - \frac{\pi\alpha}{8} - \frac{9\pi\alpha}{64}\frac{w_c}{w_{LO}}\right] \tag{5.15}$$

which implies a renormalized cyclotron mass given by

$$m^{**} = m^*\left[1 + \frac{\pi\alpha}{8} + \frac{9\pi\alpha}{64}\frac{w_c}{w_{LO}}\right] \tag{5.16}$$

The second term in (5.16) is recalled to be the contribution due to electron-LO phonon interaction. It is the third term that contains the field dependence buried in w_c. All other quantities being constant, it is evident that the effective mass should increase with increasing magnetic field. Just how well (5.16) agrees with the present experimental observations is addressed below.

To carry out the analysis on the effect of the theory, the experimental effective mass versus field data were linearly fitted and extrapolated to zero field as shown in Figure 5.9. The zero-magnetic field masses obtained were $0.0441m_e$ for sample (S-1) and $0.0380m_e$ for sample (S-2). The expected masses from (5.16) for sample (S-1) are $0.0464m_e$ at 3.85 Tesla and $0.0470m_e$ at 7.55 Tesla. The change in the theoretical mass for a change of 3.7 Tesla is only $0.0006m_e$ compared to the experimentally observed $0.012m_e$ variation. For sample (S-2), the

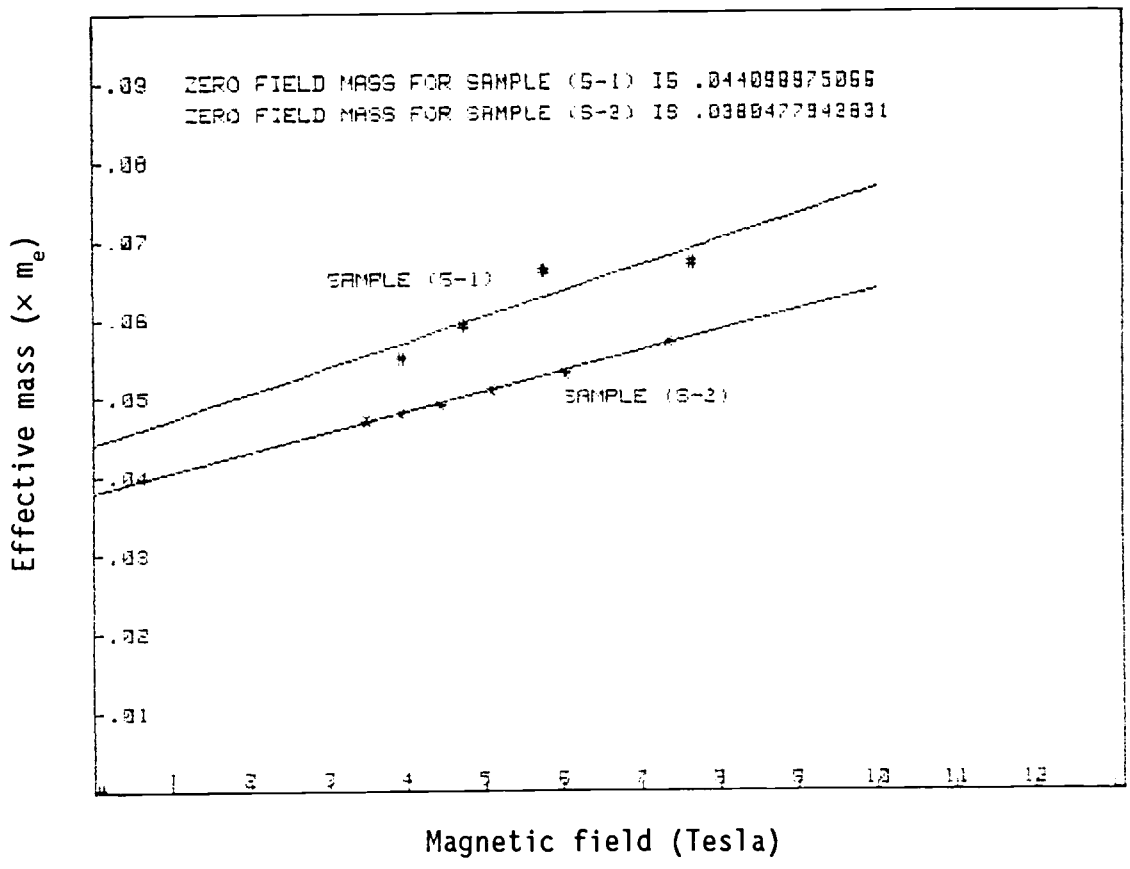

Figure 5.9 Experimental effective mass versus magnetic field for samples (S-1) and (S-2). The data points of Tables 5.1 and 5.2 were linearly fitted and extrapolated to zero-field.

expected theoretical mass for the extreme fields investigated are $0.0400m_e$ and $0.0406m_e$ for fields of 3.41 Tesla and 7.27 Tesla, respectively. Again, while the theoretical mass result varies only by $0.0006\ m_e$ for a field variation of 3.86 Tesla, the experimental result varies by a factor which is two orders of magnitude higher. These observations clearly indicate that the outlined theory alone cannot explain the observed variations.

It turns out that other factors like the sensitivity of the effective mass to variations in the oscillations amplitude and temperature are very important. To see how important these factors are, results for sample (S-1) at 5.67 Tesla were chosen for analysis. From Table 5-1, the experimental effective mass for this field was $0.066m_e$. A positive shift in all the temperature values by 0.5 °K, except by 0.1 for the lowest temperature, resulted in a mass decrease to $0.064m_e$. An equal negative shift increased the mass to $0.069m_e$. When the temperatures were shifted in the positive direction by 1 °K, the mass dropped to $0.061m_e$. A temperature shift on the order of 1 °K was not uncommon for the present experiment. For one thing the thermocouple was mounted on the back of the sample header and not directly on the sample.

The sensitivity to variations in amplitude were checked by keeping the temperatures constant and shifting the amplitudes. A positive amplitude shift of 0.03 resulted in a mass decrease to $0.061m_e$ while a corresponding negative shift increased the mass to $0.071m_e$. The choice for a shift of 0.03 was mostly judgemental but will be justified subsequently. The expression for the amplitude in (2.58) should only be good for low fields where $w_c\tau<1$. The lowest field employed in the present analysis was 3.41 Tesla which corresponds to $w_c\tau = 6.82$, assuming

a mobility of 20,000 $cm^2/V\text{-}s$. This value of $w_c\tau$ does not satisfy the mentioned condition and one expects the amplitudes to be not correctly given by (2.58). This point received considerable attention in the paper by Khalid et al.[42] in which they studied the de Haas-Van Alphen effect in Mercury. Their high magnetic field amplitude results showed departures from the semi-classical result of Lifshitz and Kosevich, the same expression used here (2.58), but considerable agreement with a many-body theory formulated by Engelsberg and Simpson (see Engelsberg & Simpson in Ref. 42). In particular the many-body theory predicts a 9% enhancement in amplitude for a field of 5 Tesla. A shift of 0.03 for a field of 5.67 Tesla corresponds to 13% enhancement for the lowest amplitude used in the analysis and is therefore not unreasonable compared with the findings of the theory.

VI. SUMMARY

Transport properties of a two-dimensional electron gas formed at an $In_xGa_{1-x}As/Al_yGa_{1-y}As$ heterojunction were investigated for two samples with x=0.15 and x=0.25. The corresponding values of y were 0.2 and 0.25, respectively. In particular, the following quantities were determined.

1. The Hall 2-D carrier concentration was determined as a function of temperature from 2 °K to 300 °K. A dip was observed in the carrier concentration at around 145 °K. This behavior was attributed to the effects of DX-centers associated with the possible existence of parallel conduction in the AlGaAs layer.

2. Hall mobility was computed as a function of temperature from 2 °K to room temperature and the resulting curves showed typical 2-D behavior. Contrary to the expectation, sample (S-2), x=0.25, showed a higher mobility than sample (S-1), x=0.15, at all temperatures considered. It is deemed likely that sample (S-1) was of less structural quality than sample (S-2). A theoretical model based on the scattering mechanisms in the channel was developed to explain the dependence of the experimental channel mobility on temperature from 2 °K to 300 °K. The general shape of the theoretical curve was similar to the experimental curve except the former was invariably higher throughout the temperature range investigated. This may partly be due to the omission of intersubband scattering and the assumption that alloy scattering only occured in the channel. As mentioned in the analysis, alloy scattering may be operational in the AlGaAs layer since the wave functions are not totally confined to the channel but penetrate into the adjacent layers. In addition,

varying two of the adjustable parameters (alloy scattering potential and background impurity concentration) in the relaxation times for these mechanisms was shown to improve the fit between experimental and theoretical curves. The relative contributions of the various scattering mechanisms to the mobility varied throughout the temperature range investigated. Alloy scattering and remote impurity scattering were found to be dominant at low temperatures while optical phonon was the limiting factor at high temperatures.

3. The effective mass of channel electrons was determined from the temperature dependence of the SdH oscillations amplitude. The masses obtained showed a positive coefficient magnetic field dependence. A theoretical explanation based on the magneto-polaron effect was investigated to explain this field dependence, but the effects of the the theory were found to be too small. Experimental errors such as inaccuracy in measuring the temperature and amplitude were found to be significant.

In order to clearly see the magnetic field dependence proposed by the many body theory of Das Sarma, the effects of temperature and amplitude fluctuations need to be eliminated. Correct amplitudes can be obtained by employing low fields that satisfy the conditions of the Lifshitz-Kosevich expression. It was found in the present research, however, that it is very difficult to observe oscillations below 3.5 Tesla. For more reliable temperature measurements, the thermocouple should be mounted directly on the sample.

VII. BIBLIOGRAPHY

1. C.W. Tu, R.H. Hendel, and R. Dingle, "Gallium Arsenide Technology," Ed. by D.K. Ferry, Sams & Co., Ch. 4, 1985.

2. R. Dingle, H.L. Stormer, A.C. Gossard, and W. Wiegman, Appl. Phys. Lett., 33 (1978) 665.

3. H.L. Stormer, R. Dingle, A.C. Gossard, W. Wiegmann, and M.D. Sturge, Sol. State Commun.,29 (1978) 705.

4. T. Mimura, S. Hiyamizu, T. fujii, and K. Nambu, Jpn. J. Appl. Phys., 19 (1980) L225.

5. L. Esaki and R. Tsu, "Superlattice and Negative Conductivity in Semiconductors," Internal Report RC 2418, IBM Research, March 26, 1969.

6. G.C. Osbourn, J. Appl. Phys., 53 (1982) 1586.

7. P.R. Brger, K. Chang, P.K. Bhattacharya, and J. Singh, J. Vac. Sci. Technol. B5 (1987) 1162.

8. I.J. Fritz, P.L. Gourley, and L.R. Dawson, Appl. Phys. Lett., 51 (1987) 1004.

9. T.G. Anderson, G.G. Chen, V.D. Kulakovskii, A. Uddin, and J.T. Vallin, Appl. Phys. Lett. 51 (1987) 753.

10. T.G. Anderson, Z.G. Chen, V.D. Kulakovskii, A. Uddin, J.T. Vallin, Sol. State Commun., 64 (1987) 379.

11. J.E. Schirber, I.J. Fritz, L.R. Dawson, and G.C. Osbourn, Phys. Rev. B, 28 (1983) 2229.

12. J.T Ebner, Masters Thesis, Oregon State University, "The Growth of Ternary Compound Semiconductors by Molecular Beam Epitaxy", 1987.

13. T. Ando, A.B. Fowler, and F. Stern, Revs. Mod. Phys., 54 (1982) 443.

14. R.L. Anderson, Solid State Electronics, 5 (1962) 341.

15. W. Walukiewicz, H.E. Ruda, J. Lagowski, and H.C. Gatos, Phys. Rev. B, 30 (1984) 4571.

16. S. Goodnick, PhD. Thesis, Colorado State University, "Transport in Inversion Layers of MOSFETs", 1983.

17. F. Fang and W.E. Howard, Phys. Rev. Lett., 16 (1966) 797.

18. F. Stern and W.E. Howard, Phys. Rev., 163 (1967) 816.

19. P.K. Basu and K. Bhattacharya, J. Appl. Phys., 59 (1986) 992.

20. T. Ando, J. Phys. Soc. Jpn., 51 (1982) 3900.

21. G. Bastard, Appl. Phys. Lett. 43 (1983) 591.

22. P.K. Basu and B.R. Nag, Appl. Phys. Lett. 43 (1983) 689

23. P.K. Basu and B.R. Nag, Surf. Sci., 142 (1984) 256.

24. P.K. Basu and K. Bhattacharya, Phys. Status Solidi B, 128 (1985) K175.

25. C. Weisbuch, Semiconductors & Semimetals, 24 (1987) 105.

26. L. Esaki and R. Tsu, "Superlattice and Negative Conductivity in Semiconductors," Internal Report RC 2418, IBM Research, March 26, 1969.

27. R. Dingle, H.L. Stormer, A.C. Gossard, and W. Wiegman, Appl. Phys. Lett., 33 (1978) 665.

28. E.E. Mendez, IEEE J. Quantum Elec., QE-22 (1986) 1720.

29. I.J. Fritz, L.R. Dawson, and T.E. Zipperian, J. Vac. Sci. Technol. B, (1983) 387.

30. S. Hiyamizu, Surf. Sci., 170 (1986) 727.

31. T. Henderson, M.I. Aksun, C.K. Peng, H. Morkoc, P.C. Chao, P.M. Smith, K.H.G. Duh, and L.F. Lester, IEEE Elec. Dev. Lett., EDL-7 (1986) 649.

32. A.A. Ketterson, W.T. Masselink, J.S. Gedymain, J. Klem, C.K. Peng, W.F. Kopp, H. Morkoc, and K.R. Gleason, IEEE Trans. Elec. Dev., ED-33 (1986) 564.

33. G.W. Wang, Y.K. Chen, D.C. Radulescu, and L.F. Eastman, IEEE Elec. Dev. Lett., 9 (1988) 4.

34. Y.K. Chen, D.C. Radulescu, G.W. Wang, F.E. Najjar, and L.F. Eastman, IEEE Elec. Dev. Lett., 9 (1988) 1.

35. A. Ketterson, M. Moloney, W.T. Masselink, C.K. Peng, J. Klem, R. Fischer, W. Kopp, and H. Morkoc, IEEE Elec. Dev. Lett., EDL-6 (1985) 628.

36. L.D. Nguyen, W.J. Schaff, P.J. Tasker, A.N. Lepore, L.F. Palmateer, M.C. Foisy, and L.F. Eastman, IEEE Trans. Elec. Dev., 35 (1988) 139.

37. J.B. Restorff, B. Houston, R.S. Allgaier, M.A. Littlejohn, S.B. Phatak, J. Appl. Phys. 51 (1980) 2277.

38. R.J. Nichols, J.C. Portal, C. Houlbert, P. Perrier, and T.P. Pearsall, Appl. Phys. Lett., 34 (1979) 492.

39. H.A. Washburn and J.R. Sites, Surf. Sci., 73 (1978) 537.

40. I.J. Fritz, J.E. Schirber, E.D. Jones, T.J. Drummond and G.C. Osbourn, Symp. GaAs and Related Compounds, Las Vegas, Nevada, 1986, Ch. 4.

41. J.E. Schirber, I.J. Fritz, and L.R. Dawson, Appl. Phys. Lett., 46 (1985) 187.

42. M.A. Khalid, P.H.P. Reinders, and M. Springford, J. Phys. F: Met. Phys., 18 (1988) 1949.

43. R.J. Sladek, Phys. Rev., 110 (1958) 817.

44. J.A. Brum and G. Bastard, Sol. State Commun., 53 (1985) 727.

45. G. Bastard, Surf. Sci., 142 (1984) 284.

46. An-Ban Chen, S. Krishnamurthy, and A. Sher, Appl. Phys. Lett., 47 (1985) 160.

47. M.A. Littlejohn, J.R. Hauser, T.H. Glisson, D.K. Perry, J.W. Harrison, Sol. State Commun., 21 (1978) 107.

48. J.W. Harrison and J.R. Hauser, Phys. Rev.B, 13 (1976) 5347.

49. J.H. Marsh, Appl. Phys. Lett., 41 (1982) 732.

50 H.A. Washburn, J.R. Sites, and H.H. Wieder, J. Appl. Phys., 50 (1979) 4872.

51 S.M. Goodnick and P. Lugli, Phys. Rev.B, 37 (1988) 2578.

52 F.F. Fang, A.B. Fowler, and A. Hartstein, Phys. Rev.B, 16 (1977) 4446.

53 S. Hiyamizu, J. Saito, K. Kondo, T. Yamamoto, T. Ishikawa, and S. Sasa, J. Vac. Sci. Technol., B3 (1985) 585

54 E.E. Mendez, P.J. Price, and M. Hieblum, Appl. Phys. Lett., 45 (1984) 294.

55 T.P. Pearshall, "GaInAsP Alloy Semiconductors", John Wiley & Sons Ltd., (1982) 225.

56 G. Gregoris, J. Beerens, S. Ben Amor, L. Dmowski, J.C. Portal, D.L. Sivco, and Y. Cho, Sol. State. Phys. C, 20 (1987) 425.

57 B.J.F. Lin, D.C. Tsui, M.A. Paalanen, and A.C. Gossard, Appl. Phys. Lett., 45 (1984) 695.

58 F. Fang, A.B. Fowler, and A. Hartstein, Phys. Rev. B, 16 (1977) 4446.

59 S. Das Sarma, Phys. Rev. B, 27 (1982) 2590.

60 S. Das Sarma, Phys. Rev. Lett., 52 (1984) 859.

61 R.L. Anderson, IBM J. Res. Dev., 4 (1960) 283.

62 S. Kawaji, J. Phys. Soc. Jpn., 27 (1967) 608.

63 H. Ezawa, T. Kuroda, and K. Nakamura, Surf. Sci., 24 (1971) 659; Surf. Sci., 27 (1971) 218.

64 C.T. Sah, T.H. Ning, and L.L. Tschopp, Surf. Sci., 32 (1972) 561.

VIII. APPENDICES

APPENDIX A

Parameters used in the derivation of the theoretical mobilities of Figure 5.1 (sample (S-1))

Remote impurity concentration	$1 \times 10^{18}/cm^3$
Background impurity concentration	$4.35 \times 10^{16}/cm^3$
Density of interface states	$1 \times 10^{10}/cm^2$
Correlation length, L	15 Å
rms height, Δ	3 Å
Fluctuating alloy scattering potential	0.6 eV
LO-phonon energy	34.2 eV
Velocity of sound	5.10×10^5 cm/s
Electron effective mass	$0.06\ m_e$
High frequency dielectric constant	11.04
Low frequency dielectric constant	13.16
Density	$5.36 \times 10^3\ Kg/m^3$
Deformation potential	7.0 eV
Spacer layer thickness	35 Å

APPENDIX B

Parameters used in the derivation of the theoretical mobilities of Figure 5.2 (sample (S-2))

Remote impurity concentration	$2 \times 10^{18}/cm^3$
Background impurity concentration	$5 \times 10^{15}/cm^3$
Density of interface states	$1 \times 10^{10}/cm^2$
Correlation length, L	15 Å
rms height, Δ	3 Å
Fluctuating alloy scattering potential	0.6 eV
LO-phonon energy	33.7 eV
Velocity of sound	5.02×10^5 cm/s
Electron effective mass	0.055 m_e
High frequency dielectric constant	11.12
Low frequency dielectric constant	13.32
Density	5.395×10^3 Kg/m^3
Deformation potential	7.0 eV
Spacer layer thickness	30 Å